THE JOURNAL OF PHYSICAL CHEMISTRY A
A JOURNAL OF THE AMERICAN CHEMICAL SOCIETY

pubs.acs.org/JPCA Article

Extension of the Variational Free Energy Profile and Multistate Bennett Acceptance Ratio Methods for High-Dimensional Potential of Mean Force Profile Analysis

Timothy J. Giese, Şölen Ekesan, and Darrin M. York*

Cite This: J. Phys. Chem. A 2021, 125, 4216–4232 Read Online

ACCESS | Metrics & More | Article Recommendations

ABSTRACT: We redevelop the variational free energy profile (vFEP) method using a cardinal B-spline basis to extend the method for analyzing free energy surfaces (FESs) involving three or more reaction coordinates. We also implemented software for evaluating high-dimensional profiles based on the multistate Bennett acceptance ratio (MBAR) method which constructs an unbiased probability density from global reweighting of the observed samples. The MBAR method takes advantage of a fast algorithm for solving the unbinned weighted histogram (UWHAM)/MBAR equations which replaces the solution of simultaneous equations with a nonlinear optimization of a convex function. We make use of cardinal B-splines and multiquadric radial basis functions to obtain smooth, differentiable MBAR profiles in arbitrary high dimensions. The cardinal B-spline vFEP and MBAR methods are compared using three example systems that examine 1D, 2D, and 3D profiles. Both methods are found to be useful and produce nearly indistinguishable results. The vFEP method is found to be 150 times faster than MBAR when applied to periodic 2D profiles, but the MBAR method is 4.5 times faster than vFEP when evaluating unbounded 3D profiles. In agreement with previous comparisons, we find the vFEP method produces superior FESs when the overlap between umbrella window simulations decreases. Finally, the associative reaction mechanism of hammerhead ribozyme is characterized using 3D, 4D, and 6D profiles, and the higher-dimensional profiles are found to have smaller reaction barriers by as much as 1.5 kcal/mol. The methods presented here have been implemented into the FE-ToolKit software package along with new methods for network-wide free energy analysis in drug discovery.

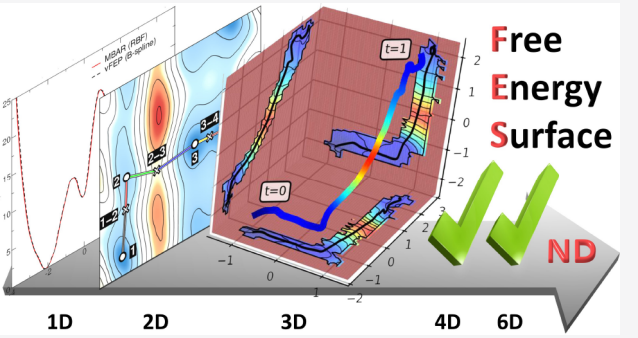

INTRODUCTION

Chemical processes are driven by changes in free energy and can be studied using molecular simulations that can predict these changes and provide a molecular-level understanding to help guide design.[1−4] There are several types of free energy calculations encountered in the field of computational chemistry. Among the most common are so-called alchemical free energy methods[2,4] that utilize the state property of the free energy to determine thermodynamic changes between two states using a nonphysical (i.e., "alchemical") pathway. For many other applications, the desired goal is to determine the mechanism of a chemical process, that is, the likely pathway (or set of pathways) that physically connects the states, including the location of key transition states and intermediates, and determining factors that regulate the rates and outcomes of the process. Examples include transitions between conformational states,[5−12] association/binding events,[13−21] traversal of ions through channels and membranes,[22−25] and enzymatic and nonenzymatic chemical reactions in the condensed phase.[26−32] One way of characterizing such mechanisms is through the construction of a *free energy surface* (FES) or related *potential of mean force* (PMF), in a reduced coordinate space (henceforth referred to as "reaction coordinates") that provides a practical basis for interpretation.[15,33−35] FESs are also referred to as *free energy profiles*, and these terms are used interchangeably. We will henceforth use FES as an acronym to refer to free energy surface/profile rather than "FEP" so as to avoid confusion with the acronym "vFEP" (which stands for variational free energy profile and refers to one of the main methods being developed herein).

Free energy profiles are derived from the analysis of sets of enhanced sampling simulations. A common enhanced sampling strategy is to introduce biasing potentials that

Received: January 26, 2021
Revised: March 9, 2021
Published: March 30, 2021

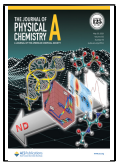

https://doi.org/10.1021/acs.jpca.1c00736
J. Phys. Chem. A 2021, 125, 4216−4232

facilitate transitions over barriers that would otherwise be prohibited or only very sparsely sampled. In this way, the methods help to establish more uniform coverage of the relevant configurational space. The most common approach is to use sets of "umbrella sampling" simulations,[36,37] where the biasing potential is a harmonic (quadratic) penalty function in the space of reaction coordinates that is used to localize sampling near to the harmonic (or "umbrella") centers. Typically these simulations are carried out by having multiple umbrella potentials (umbrella centers and/or force constants) distributed so as to collectively provide statistical sampling of the important regions of the FES. Sometimes these umbrella potentials are further enhanced by additional biasing potentials that help to "flatten out" the FES so as to facilitate more uniform sampling.[38] Adaptive umbrella sampling is another method designed to improve the uniformity of the sampling[39−42] which has been found to be a cost-effective approach for characterizing high-dimensional FESs.[43]

The relevant reaction coordinates are collected from the biased simulations. This data must be analyzed to remove the bias, and represented in the form of a free energy profile. In order to convert the biased sampled fluctuation data into unbiased data, one must first locally unbias (reweight) the frames within each simulation using the appropriate inverse Boltzmann weight from the biasing potential. Next, the different simulation ensembles need to be globally reweighted using statistical methods[34,44−54] that estimate the relative free energy of each umbrella simulation. The unbiased data can then be used to construct a numerical or analytical model representation of the free energy profile in the space of the reaction coordinates. These profiles can be used to identify catalytic pathways and characterize rate-controlling transition state ensembles. Recently, free energy profiles for the twister[55] and Varkud satellite[56] ribozymes from *ab initio* combined quantum mechanical/molecular mechanical (QM/MM) simulations have been used within a computational enzymology approach[55−59] to study RNA-cleavage reactions[60] and gain insight into nucleic acid enzyme design.[61]

A number of methods have been developed to compute free energy profiles from analysis of molecular dynamics simulations, including the weighted histogram analysis method[34,44,45,62] (WHAM) and unbinned variations (UWHAM),[46] umbrella integration (UI),[47−49] multistate Bennett acceptance ratio method (MBAR),[50,51] and the vFEP method.[52−54] The latter affords some distinct advantages with respect to the ability to provide a robust, analytic representation (including derivatives with respect to reaction coordinates) of the free energy profile with minimal sampling.[52] Such an analytic representation is important for applications due to the following: (1) It enables one to efficiently search for minimum free energy pathways that connect the relevant chemical or conformational states and characterize the mechanism.[55,56] (2) It can be used in automated iterative refinement procedures to identify regions where further sampling is required.[54] (3) It can be exploited by enhanced sampling methods as an inverse biasing potential to facilitate uniform sampling on the free energy surface.[40−42] (4) It can serve as a correction potential to improve the accuracy of force fields.[63−65]

The vFEP approach has been implemented and demonstrated to be useful using a cubic spline representation for 1D[52] and 2D[53] free energy profiles. However, extension to general higher dimensions has been challenging, despite the need for such an approach for many applications, particularly path methods such as the finite temperature string[66] and nudged elastic band[67,68] methods that consider more reaction coordinates. The vFEP method tackles the problems of reweighting and analytic representation of the data simultaneously. Other methods such as MBAR formally only address the data reweighting step, and the representation of the data in terms of a robust analytic surface requires some form of fitting or interpolation in a second step. No general methods exist for determining the robust analytic representations of free energy profile data in arbitrarily high dimensions, particularly when nonuniform sampling is carried out. Herein we address these challenges by introducing new methods and novel computational tools implemented in the FE-ToolKit software package[69] and made freely available to the community for calculating free energy profiles using both MBAR and vFEP in high dimensions.

In this work, we present an extension of the vFEP method to arbitrary high dimensions using cardinal B-splines.[70] We further describe an efficient, scalable software implementation of an MBAR approach for calculating free energy profiles[51,71] that incorporates a fast solution for the MBAR/UWHAM equations to nonlinearly optimize a convex function.[46] Finally, we present a novel method for robust analytic representation of the data using multiquadric radial basis functions to obtain smooth, differentiable free energy profiles in arbitrary high dimensions from nonuniformly sampled data and fast MBAR analysis. These tools have been integrated into the ndfes program within the FE-ToolKit software package, which is freely available.[69]

We compare the MBAR and vFEP methods using several examples: (1) the 1D FES of a phosphoryl transfer reaction of a model compound with an ethoxide leaving group computed from *ab initio* QM/MM simulations, (2) periodic 2D Ramachandran FESs of alanine, glycine, and valine dipeptide computed from MM simulations, and (3) the 3D FES of the associative transphosphorylation reaction mechanism catalyzed by the hammerhead ribozyme (HHr) from semiempirical QM/MM simulations. We further explore how the HHr minimum free energy pathway is effected by increasing the dimensionality of the FES to four and six reaction coordinates.

METHODS

Variational Free Energy Profile (vFEP) Method. The vFEP method, derived in ref 52, is a procedure for obtaining an unbiased FES from a series of biased umbrella window simulations. Given the umbrella biasing potentials and the time series of observed reaction coordinate values $\{\mathbf{x}_{\mathbf{obs}}\}$ for each simulation, the goal is to construct an analytic representation of the global unbiased FES. The vFEP approach for reconstructing the global FES is to assume a model form for the reduced FES, $f(\mathbf{x}; \mathbf{p})$, that depends on the parameters $\mathbf{p}$. Reduced potential energy units of k_BT are used throughout the manuscript, where k_B is the Boltzmann constant and T is the absolute temperature, such that the inverse temperature $\beta = (k_BT)^{-1}$ does not explicitly appear. Here the argument $\mathbf{x}$ of the reduced FES model represents the N-dimensional (N_{dim}) set of reaction coordinate values that define the spanned free energy space. The model parameters that best reproduce the global FES, $\mathbf{p}^*$, are those that minimize the objective function shown in eq 2.

https://doi.org/10.1021/acs.jpca.1c00736
J. Phys. Chem. A 2021, 125, 4216−4232

$$\mathbf{p}^* = \arg\min_{\mathbf{p}}\{O(\mathbf{x_{obs}};\, \mathbf{p})\} \tag{1}$$

$$O(\mathbf{x_{obs}},\, \mathbf{p}) = \sum_{a=1}^{N_{sim}} \ln Z_a(\mathbf{p}) + \sum_{a=1}^{N_{sim}} N_a^{-1} \sum_{i=1}^{N_a} g_{ai} f(\mathbf{x}_{\mathbf{obs},ai};\, \mathbf{p}) \tag{2}$$

N_{sim} is the number of umbrella window simulations. N_a is the number of observations drawn from simulation a. $\mathbf{x}_{\mathbf{obs},ai}$ is the array of reaction coordinate values of sample i within simulation a. $Z_a(\mathbf{p})$ is a configurational integral of simulation a.

$$Z_a(\mathbf{p}) = \int \cdots \int e^{-[f(\mathbf{x};\mathbf{p})+w_a(\mathbf{x})]}\, dx_1 \cdots dx_{N_{dim}} \tag{3}$$

$w_a(\mathbf{x})$ is the umbrella biasing (reduced) potential used in simulation a. The formulation presented in this manuscript does not presume a form for the umbrella biasing potential, but it is common for it to be a sum of N_{dim} uncoupled harmonic oscillators centered about $x_{0,d}$ with force constants k_d, where N_{dim} is the number of reaction coordinates.

$$w_a(\mathbf{x}) = \sum_{d=1}^{N_{dim}} k_d (x_d - x_{0,d})^2 \tag{4}$$

In some cases, an additional biasing potential is introduced to attempt to flatten out the free energy surface in the space of the reaction coordinates such that sampling within different umbrella windows is more uniform. In fact, such a biasing potential can be derived from a rough estimate of $-f(\mathbf{x};\, \mathbf{p}^*)$ itself (e.g., from coarse-grained sampling).[38]

The g_{ai} quantity appearing in eq 2 is a minor generalization of the original vFEP method in the present work to reweight trajectories to remove the effect of additional restraint potentials (not directly involving the reaction coordinates) on the FES. Specifically, this term is the degeneracy of sample i drawn from simulation a. If the umbrella window simulations are unencumbered by additional restraints (and hence there is no additional restraint bias that requires reweighting), then the degeneracy of each frame is unity ($g_{ai} = 1$); however, if the additional bias introduced by a reduced restraint potential $u_{rest,ai}$ needs to be removed, then the sample degeneracy is given by eq 5.

$$g_{ai} = N_a \frac{e^{u_{rest,ai} - u_{max}}}{\sum_{j=1}^{N_a} e^{u_{rest,aj} - u_{max}}} \tag{5}$$

Formally, the value of u_{max} has no effect; in practice, one chooses u_{max} to be the maximum observed value of $u_{rest,ai}$ to prevent overflow of the exponential function.

In the present work, we describe a vFEP implementation that can be solved for arbitrarily high dimensional FESs. The main approximations of our method are as follows: (a) Space is divided into a uniform N_{dim}-dimensional grid consisting of *bins* (N_{dim}-dimensional grid "volumes") and *corners* (grid line intersections). Every bin is the same shape and size, but each dimension of a bin may have a different fixed width. (b) The FES is assumed to be positive infinity throughout space except within those bins populated by at least one sample from any simulation (that is, the probability is zero for the unoccupied bins). (c) For those regions of space populated by at least one sample, the FES is modeled by cardinal B-spline functions.[70] The values of the FES are defined by a weighted average of control parameters associated with the nearby corners, and the weights are the B-spline values evaluated at those corners. (d) The configurational integral of eq 3 is numerically evaluated from the Gauss−Legendre quadrature[72] of each bin.

Division of Space into a Uniform Grid for Nonperiodic Systems. Given a target bin width for each dimension, Δx_d, appropriate values for the grid minimum $x_{min,d}$ and the number of bins $N_{bin,d}$ in each direction are chosen such that the grid maximum is an integer multiple of the grid size $x_{max,d} = N_{bin,d}\Delta x_d + x_{min,d}$ and all observed points are enclosed within the range $\mathbf{x_{min}}$ and $\mathbf{x_{max}}$. To do this, we note the maximum and minimum coordinates from the observed samples, calculate the number of bins that can fit within that range, expand the range minimum by Δx_d, and increase the number of bins in direction d by 2. This produces a range that is guaranteed to contain all samples while also being an integer multiple of the target bin width. The range must further be padded on either side by additional bins to fully define the B-splines evaluated near the grid edges (this will depend on the order n of the B-spline used). Although the free energy is assumed to positive infinity within this buffer region, the padded bin corners contribute control parameters accessible to the nonbuffer region. Specifically, the ranges must be extended by an additional $N_{bin,d}^{buf} = \lfloor (n+1)/2 \rfloor - 1$ bins on both sides (where $\lfloor x \rfloor$ denotes the *floor* function of x, i.e., the largest integer $\leq x$), such that the bin counts increase by $2N_{bin,d}^{buf}$. For example, for a B-spline order of $n = 5$ or 6, $N_{bin,d}^{buf} = 2$. Application of this procedure to each dimension creates a grid consisting of $N_{bin} = \prod_{d=1}^{N_{dim}} N_{bin,d}$ bins and $N_c = \prod_{d=1}^{N_{dim}} (N_{bin,d} + 1)$ corners; however, many bins will be unoccupied by samples, so only a petite list of occupied bins need to be tracked.

Division of Space into a Uniform Grid for Periodic Systems. For periodic systems, one specifies a number of bins, N_{bin}, from which the target bin width is determined so as to obey the periodicity of the system. Hence, for a periodic interval of 2π, the bin width is $\Delta x_d = 2\pi/N_{bin}$. Unlike the nonperiodic case, there is no need to pad the grid; rather, the B-spline weights are simply "wrapped" to the appropriate interval of periodic grid points.

Cardinal B-Splines. The model form of the reduced free energy is a weighted average of the B-spline control parameters p_c associated with the grid corners, and the weights are the cardinal B-spline values evaluated at the corner positions, $\mathbf{x}_c$

$$f(\mathbf{x};\, \mathbf{p}) = \sum_{c=1}^{N_c} \theta_n(\mathbf{x}_{c,c} - \mathbf{x}) p_c \tag{6}$$

where $\theta_n(\mathbf{x} - \mathbf{x}_p)$ is a N_{dim}-dimensional cardinal B-spline of order n centered about the point $\mathbf{x}_p$

$$\theta_n(\mathbf{x} - \mathbf{x}_p) = \prod_{d=1}^{N_{dim}} M_n\left(N_{bin,d} \frac{x_d - x_{p,d}}{x_{max,d} - x_{min,d}} + \frac{n}{2} \right) \tag{7}$$

and M_n is given by eq 8.

$$M_n(u) = \frac{1}{(n-1)!} \sum_{k=0}^{n} (-1)^k \binom{n}{k} [\max(u-k, 0)]^{n-1} \tag{8}$$

Cardinal B-splines have compact support; that is, they are nonzero only within a well-defined range. Only the nearest $N_{near,d} = 2\lfloor (n+1)/2 \rfloor$ corners in each dimension can have a nonzero value of M_n; therefore, only $N_{near} = \prod_{d=1}^{N_{dim}} N_{near,d}$ total corners need to be considered for any FES evaluation. For example, if n is even, then M_n will be nonzero for the n nearest corners. If n is odd, then the location of the n nearest corners

https://doi.org/10.1021/acs.jpca.1c00736
J. Phys. Chem. A 2021, 125, 4216−4232

will depend on whether the evaluation point is located before or after the bin midpoint. For notational purposes, let $\hat{c}(\mathbf{x}, c)$ be an operator that accepts a point in space $\mathbf{x}$ and an integer in the range $c \in [1, N_{\text{near}}]$ and returns the global index of a nearby corner. Equation 6 can then be rewritten to emphasize the B-spline's compact support, when appropriate.

$$f(\mathbf{x};\, \mathbf{p}) = \sum_{c=1}^{N_{\text{near}}} \theta_n(\mathbf{x}_{\mathbf{c},\hat{c}(\mathbf{x},c)} - \mathbf{x}) p_{\hat{c}(\mathbf{x},c)} \tag{9}$$

Inserting eq 6 into eq 2 yields

$$O(\mathbf{x}_{\mathbf{obs}},\, \mathbf{p}) = \sum_{a=1}^{N_{\text{sim}}} \ln Z_a(\mathbf{p}) + \sum_{c=1}^{N_c} p_c h_c \tag{10}$$

where h_c arises from regrouping of parentheses.

$$h_c = \sum_{a=1}^{N_{\text{sim}}} N_a^{-1} \sum_{i=1}^{N_a} g_{ai}\, \theta_n(\mathbf{x}_{\mathbf{c},c} - \mathbf{x}_{\mathbf{obs},ai}) \tag{11}$$

The h_c values can be precomputed and stored at the start of the nonlinear optimization procedure to eliminate B-spline evaluations for every observed data point in each optimization step.

Numerical Integration of Z_a. Gauss−Legendre quadrature is an efficient numerical solution for integration in the range $[-1, 1]$.[72]

$$\int_{-1}^{1} f(x)\, \mathrm{d}x = \sum_{i=1}^{N_{\mathrm{q},d}} w_{\mathrm{q},i} f(x_{\mathrm{q},i}) \tag{12}$$

The $x_{\mathrm{q},i}$ values are the roots of a Legendre polynomial of order $N_{\mathrm{q},d}$, $P_{N\mathrm{q},d}(x)$, and the weights are $w_{\mathrm{q},i} = 2/\{(1-x_{\mathrm{q},i}^2)\text{-}P'_{N_{\mathrm{q},d}}(x_{\mathrm{q},i})]^2\}$. The range of integration is easily adjusted via u substitution; an integral over the range $[-\Delta x/2, \Delta x/2]$ merely requires scaling of $w_{\mathrm{q},i}$ and $x_{\mathrm{q},i}$ by $2/\Delta x$. Integration in multiple dimensions leads to an analogous summation over a mesh of $N_{\mathrm{q}} = \prod_{d=1}^{N_{\text{dim}}} N_{\mathrm{q},d}$ quadrature points $\mathbf{x}_{\mathbf{q}}$, whose weights are an outer-product of appropriately scaled, 1D weights. The configurational integral, Z_a, evaluated over all-space can be replaced by the sum of N_{dim}-dimensional Gauss−Legendre quadratures, each integrating the volume of an occupied bin.

$$\begin{aligned} Z_a(\mathbf{p}) &= \sum_{b=1}^{N_{\text{bin}}} \int_{-\Delta x_1/2+x_{\mathrm{b},1}}^{\Delta x_1/2+x_{\mathrm{b},1}} \cdots \int_{-\Delta x_{N_{\text{dim}}}/2+x_{\mathrm{b},N_{\text{dim}}}}^{\Delta x_{N_{\text{dim}}}/2+x_{\mathrm{b},N_{\text{dim}}}} \mathrm{e}^{-f(\mathbf{x};\mathbf{p})-w_a(\mathbf{x})}\, \mathrm{d}x_1 \cdots \mathrm{d}x_{N_{\text{dim}}} \\ &= \sum_{b=1}^{N_{\text{bin}}} \sum_{i=1}^{N_{\mathrm{q}}} E_{aib}\, \mathrm{e}^{-f_{ib}(\mathbf{p})} \end{aligned} \tag{13}$$

The quadrature weights and umbrella biasing potential exponential have been absorbed into a single term $E_{aib} = w_{\mathrm{q},i}\, \mathrm{e}^{-w_a(\mathbf{x}_{\mathrm{q},i}+\mathbf{x}_{\mathrm{b},b})}$, $\mathbf{x}_{\mathbf{b},b}$ is the center of bin b, and $f_{ib}(\mathbf{p})$ is a shortened notation for eq 14.

$$f_{ib}(\mathbf{p}) = f(\mathbf{x}_{\mathbf{q},i} + \mathbf{x}_{\mathbf{b},b};\, \mathbf{p}) \tag{14}$$

In our notation, the mesh of quadrature points $\mathbf{x}_{\mathbf{q},i}$ is the same for each bin (ranging from $-\Delta\mathbf{x}/2$ to $\Delta\mathbf{x}/2$); the only spatial difference between the local quadrature meshes are the location of their bin centers. Consequently, the B-spline evaluations can be precomputed as a matrix for a single, prototype bin centered at the origin, and the FES evaluation at the quadrature mesh points becomes matrix−vector product between the prototype B-spline weight matrix and the petite list of nearby corner parameters.

$$f_{ib}(\mathbf{p}) = \sum_{c=1}^{N_{\text{near}}} T_{ic} p_{\hat{c}(\mathbf{x}_{\mathbf{b},b},c)} \tag{15}$$

$$T_{ic} = \theta_n(\tilde{\mathbf{x}}_{\mathbf{c},c} - \mathbf{x}_{\mathbf{q},i}) \tag{16}$$

The $\tilde{\mathbf{x}}_{\mathbf{c},c}$ values are the positions of the N_{near} nearby corners about the prototype bin centered at the origin.

Within the context of the numerical optimization procedure, the computational scaling of the cardinal B-spline vFEP objective function is $O(N_{\text{bin}}(nN_{\mathrm{q},d})^{N_{\text{dim}}} + N_{\text{sim}}N_{\text{bin}}N_{\mathrm{q},d}^{N_{\text{dim}}})$, where n is the B-spline order and $N_{\mathrm{q},d}$ is the quadrature rule in each dimension. The scaling behavior is dominated by the calculation of the Z_a values. The $(nN_{\mathrm{q},d})^{N_{\text{dim}}}$ component of the scaling is the evaluation of the reduced free energy at each quadrature point (eq 15) within one bin. The scaling is proportional to N_{bin} because each occupied bin contributes to the integration. The second term in the scaling expression corresponds to the double summation in eq 13 for each of the N_{sim} configuration integrals. In practice, the number of occupied bins that need to be integrated does not scale proportionally to the number of simulations, because there is often some overlap between the simulated distributions. Furthermore, distant bins (relative to the umbrella window center) do not significantly contribute to the configuration integral because the umbrella biasing potential becomes very large and thus the integrand becomes very small. One should therefore expect the scaling to be proportional to N_{sim} rather than N_{sim}^2 in practice.

Parameter Gradients. Some nonlinear optimization methods require the derivative of the objective function with respect to the parameters. These gradients are given by eqs 17−19.

$$\frac{\partial O}{\partial p_c} = h_c - \sum_{a=1}^{N_{\text{sim}}} Z_a^{-1} \frac{\partial Z_a}{\partial p_c} \tag{17}$$

$$\frac{\partial Z_a}{\partial p_c} = -\sum_{b=1}^{N_{\text{bin}}} \sum_{i=1}^{N_{\mathrm{q}}} E_{aib}\, \mathrm{e}^{-f_{ib}(\mathbf{p})} f_{ib}(\mathbf{p}) \frac{\partial f_{ib}}{\partial p_c} \tag{18}$$

$$\frac{\partial f_{ib}}{\partial p_c} = \theta_n(\mathbf{x}_{\mathbf{c},c} - \mathbf{x}_{\mathbf{q},i} - \mathbf{x}_{\mathbf{b},b}) = \begin{cases} T_{ie} & \text{if } c = \hat{c}(\mathbf{x}_{\mathbf{b},b},\, e) \\ 0 & \text{otherwise} \end{cases} \tag{19}$$

High-Dimensional Free Energy Profiles Using the Multistate Bennett Acceptance Ratio Method. We have also implemented an algorithm for producing arbitrarily high dimensional FESs using the multistate Bennett acceptance ratio (MBAR) formalism, described in ref 51. In this approach, the reduced free energy is computed for each bin from an unbiased probability density obtained from reweighting the observed samples. The expression for the reduced free energy at the bin center (eq 20) makes use the *indicator function* (eq 21), which acts to select the frames within the volume of the bin.

https://doi.org/10.1021/acs.jpca.1c00736
J. Phys. Chem. A 2021, 125, 4216−4232

$$f(\mathbf{x}_{\mathbf{b},b}) = -\ln \sum_{a=1}^{N_{\text{sim}}} \sum_{i=1}^{N_a} \frac{1_{[\mathbf{x}_{\mathbf{b},b}-\Delta\mathbf{x}/2,\mathbf{x}_{\mathbf{b},b}+\Delta\mathbf{x}/2]}(\mathbf{x}_{\mathbf{obs},ai})}{\sum_{a'=1}^{N_{\text{sim}}} N_{a'} e^{-f_{a'}-w_{a'}(\mathbf{x}_{\mathbf{obs},ai})}} \tag{20}$$

$$1_{[\mathbf{x}_L,\mathbf{x}_H]}(\mathbf{x}) = \begin{cases} 1 & \text{if } x_{L,d} \le x_d < x_{H,d} \ \forall\ d \\ 0 & \text{otherwise} \end{cases} \tag{21}$$

The f_a values appearing in eq 20 are the reduced free energy of each biased simulation. Formally, the f_a values can be obtained from self-consistent solution of the coupled MBAR equations (eq 22); however, our implementation solves the MBAR/UWHAM equations[46,50,71,73,74] (eqs 23 and 24), which were first derived in ref 46. The MBAR/UWHAM method benefits from leveraging existing nonlinear parameter optimization software to obtain a solution.

$$e^{-f_t} = \sum_{a=1}^{N_{\text{sim}}} \sum_{i=1}^{N_a} \frac{e^{-w_t(\mathbf{x}_{\mathbf{obs},ai})}}{\sum_{a'=1}^{N_{\text{sim}}} N_{a'}\, e^{-f_{a'}-w_{a'}(\mathbf{x}_{\mathbf{obs},ai})}} \tag{22}$$

In the present context, the MBAR/UWHAM method minimizes the objective function shown in eq 23 with respect to the b_a parameters. The f_a values are then obtained from eq 24.

$$O(\mathbf{b}) = \frac{1}{N} \sum_{a=1}^{N_{\text{sim}}} \sum_{i=1}^{N_a} \ln\left(\sum_{a'=1}^{N_{\text{sim}}} e^{-w_{a'}(\mathbf{x}_{\mathbf{obs},ai})-b_{a'}} \right) + \sum_{a=1}^{N_{\text{sim}}} \frac{N_a}{N} b_a \tag{23}$$

$$f_a = -\ln \frac{N_a}{N} - b_a \tag{24}$$

The $N = \sum_{a=1}^{N_{\text{sim}}} N_a$ quantity appearing in eqs 23 and 24 is the total number of observations drawn from all umbrella window simulations.

Within the context of the numerical optimization procedure, the computational scaling of the MBAR/UWHAM objective function is $O(N_a N_{\text{sim}}^2)$, where N_a is the number of samples per simulation. The scaling is dominated by the calculation of the first term in eq 23.

The MBAR free energy values (eq 20) are obtained from histogram binning. To view the free energy as a surface, one could assume the value of the free energy is a constant within each bin; however, this would make it difficult to use the surface for obtaining minimum free energy paths. A better approach is to assume the computed values are the free energies at the histogram bin centers and then construct a continuous surface by interpolating between the bin centers. An appropriate choice for the interpolating function depends on factors such as whether the reaction coordinates are periodic or if the available data forms a regular grid. For example, if the MBAR histogram bin centers form a complete uniform grid over a periodic range, then cardinal B-splines are good interpolation functions, because they offer compact support and the spline coefficients can be easily determined. The B-spline coefficients that reproduce the free energy values are the reverse Fourier transform of the ratio between the free energy's Fourier coefficients and the B-spline function's Fourier coefficients.[63,75] If the histogram centers do not form a complete uniform grid, then the data is "scattered", and the cardinal B-spline representation is not well suited. However, a smooth, differentiable interpolation of scatter data can be constructed using *multiquadric radial basis functions* (RBFs).[76,77] A radial basis function is any function that satisfies $\varphi(\mathbf{x}) = \varphi(\|\mathbf{x}\|)$, where $\|\cdot\|$ returns the Euclidean distance of a vector. The multiquadric radial basis function is the particular form of $\varphi(\mathbf{x})$ shown in eq 25.

$$\varphi(r) = \sqrt{1 + (\epsilon r)^2} \tag{25}$$

The ϵ value is a "shape parameter". The optimal choice of the shape parameter is a subject of active research[77−79] which has led to a number of heuristics for choosing its value; however, it remains quite common to choose an acceptable value from trial and error.[79] Our experience is that $\epsilon = 10$ yields good interpolations for the free energy surfaces we have studied. Small values of ϵ may lead to interpolations that display unphysical oscillations. Radial basis functions are advantageous because few restrictions are placed on the data to be interpolated. The data does not need to be uniformly distributed, and their locations can be of any dimensionality. The disadvantage of RBFs is that they become expensive to evaluate as the amount of input scatter data increases. This expense is not a significant issue when applied to MBAR because RBF evaluations are not required to evaluate eqs 20 and 23; the RBFs are only used to interpolate the data to create an analytic representation. The expense associated with RBFs do not make them an ideal model for solving the vFEP equations, however, because the numerical integration of the configuration integral would require their re-evaluation within every step of the vFEP objective function optimization.

The interpolation of scattered MBAR free energies at an arbitrary position, $\mathbf{x}$, is a weighted sum of multiquadric radial basis functions evaluated at the histogram centers, $\mathbf{x}_{\mathbf{b},b}$.

$$f(\mathbf{x}) = \sum_{b=1}^{N_{\text{bin}}} m_b \varphi(\|\mathbf{x}_{\mathbf{b},b} - \mathbf{x}\|) \tag{26}$$

The weights are chosen by solving a set of linear equations that guarantee reproduction of the free energy values at each histogram center.

$$m_b = \sum_{b'=1}^{N_{\text{bin}}} A_{bb'}^{-1} f(\mathbf{x}_{\mathbf{b},b'}) \tag{27}$$

The solution for the weights is unique if the interpolation matrix (eq 28) is nonsingular.

$$A_{bb'} = \varphi(\|\mathbf{x}_{\mathbf{b},b} - \mathbf{x}_{\mathbf{b},b'}\|) \tag{28}$$

The multiquadric radial basis functions are positive-definite functions, making it unlikely to encounter a singular interpolation matrix, in practice.

In summary, the MBAR method addresses reweighting of the data to obtain free energy values within occupied bins. As a second step, the binned values must be represented using analytic functions to analyze the FES. The analysis of the FES often includes the determination of pathways and stationary points that provide insight into mechanism. The analytic model of the FES could potentially be exploited to enhance sampling or correct potential functions. We have described general procedures for creation of an analytic FES from MBAR data using either B-splines (for uniform grid data) or RBFs (for "scattered" data).

Computational Details. We carried out simulations of three sets of systems to generate data used to compare the vFEP and MBAR FES analysis methods. A description of the simulations is provided here. For 1D surfaces, umbrella window simulations were carried out of a model phosphoryl

https://doi.org/10.1021/acs.jpca.1c00736
J. Phys. Chem. A 2021, 125, 4216−4232

transesterification reaction with an ethoxide leaving group (Figure 1).

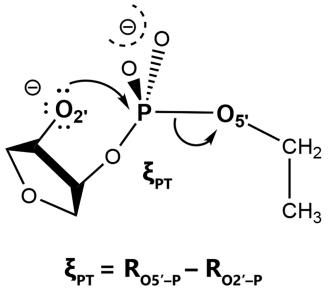

Figure 1. Model phosphoryl transfer reaction with an ethoxide leaving group and the reaction coordinate studied.

The reaction coordinate, ξ_{PT}, is the difference in distances $R_{P-O5'} - R_{P-O2'}$, which was sampled from −4 to 5 Å using 91 umbrella window QM/MM simulations. The solute was treated with the PBE0/6-31G* hybrid density functional method,[80,81] and the solvent was modeled with 1510 TIP4P/Ew water molecules.[82] The system density was equilibrated at a constant pressure of 1 atm, and the production simulations were carried out at constant volume and temperature (298 K) using a Langevin thermostat. A 50 kcal mol^{-1} Å^{-2} umbrella potential force constant was used, and each simulation was carried out for 25 ps using a 1 fs time step. The reaction coordinate was saved every 25 frames. The Lennard-Jones potential was cutoff at 9 Å, and a long-range tail correction was used to model the LJ interactions beyond the cutoff. Long-range electrostatics were treated with the ambient potential composite Ewald method.[83]

For 2D surfaces, we carried out a series of umbrella window simulations that explore the glycine, alanine, and valine dipeptide FESs with respect to the ϕ and ψ peptide dihedral angles. The dipeptide solute was modeled with the Amber ff14SB force field[84] solvated by 1398 (alanine), 1493 (valine), or 1335 (glycine) TIP4P/Ew waters.[82] A 45-by-45 array of umbrella window simulations that sample the ϕ and ψ coordinates every 8° (from 0 to 352°) were carried out using an umbrella force constant of 200 kcal mol^{-1} rad^{-2} for each coordinate. Each production simulation was run in the isothermal−isobaric ensemble using the Langevin thermostat and Berendsen barostat to maintain 298 K and 1 bar for 200 ps. The simulations were carried out with a 2 fs time step and hydrogen mass repartitioning to allow for a larger time step. The reaction coordinates were recorded every 1000 steps. The Lennard-Jones potential was truncated at 8 Å, and a long-range tail correction was used to model the LJ interactions beyond the cutoff. Long-range electrostatics were treated with the particle mesh Ewald (PME) method.[85,86]

For 3D, 4D, and 6D surfaces, we carried out simulations to characterize the associative transphosphorylation reaction mechanism catalyzed by the hammerhead ribozyme (HHr), where residues G8 and G12 act as the general acid and base, respectively. The mechanism is depicted in Figure 2. The HHr system was built starting from the crystal structure[87] (Protein Data Bank ID: 2OEU). The Mn^{2+} ions were replaced with Mg^{2+}. The GTP-, OMC-, and 5BU-modified nucleobases were replaced with wild-type G, C, and U, respectively. The nucleophile (N-1:O2′) was deprotonated and connected to the scissile phosphate to create a transition state (TS) mimic. The

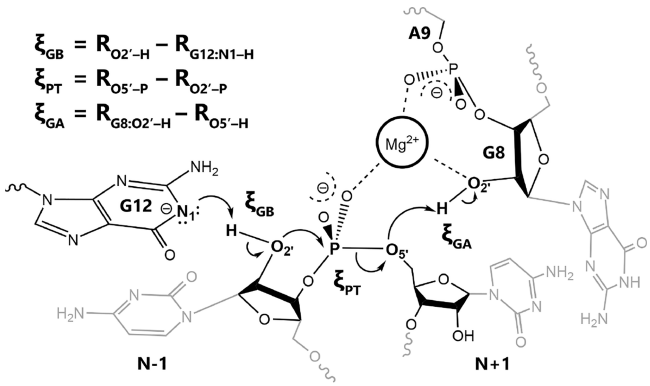

Figure 2. Associative transphosphorylation mechanism catalyzed by the hammerhead ribozyme and the three reaction coordinates used to represent progression of the general base (ξ_{GB}), phosphoryl transfer (ξ_{PT}), and general acid (ξ_{GA}) steps. Atoms in the QM and MM regions are shown as black and gray, respectively. Although not shown in the scheme to avoid crowding, the QM region additionally includes the sugar of G12, and four waters, three of which coordinate the Mg^{2+}.

system was then placed in a 85 Å truncated octahedron water box. Ions were added to balance the system charge and achieve a bulk ion concentration of 0.14 M NaCl. The solvated system was equilibrated (as described in ref 58) and simulated for 100 ns. During the simulation, the active site Mg^{2+} shifted from the crystallographic position at C-site to the B-site,[88] where it coordinates N+1:pro-R_P, A9:pro-R_P, and G8:O2′. The MM simulations were carried out using AMBER18,[89] employing the ff99OL3 RNA force field,[90,91] the TIP4P/Ew water model,[82] and the corresponding ions.[92−95] Simulations were carried out under periodic boundary conditions at 300 K using an 12 Å nonbond cutoff and PME electrostatics.[85,86] The Langevin thermostat with γ = 5 ps^{-1} and Berendsen isotropic barostat with τ = 1 ps were used to maintain a constant pressure and temperature. A 1 fs time step was used along with the SHAKE algorithm to fix hydrogen bond lengths.[96] The HHr umbrella window simulations were carried out using the AM1/d-PhoT semiempirical Hamiltonian[97] to model a QM region consisting of 89 atoms, including the following: the scissile phosphate and flanking sugars, the G12 nucleobase and sugar, the G8 sugar, the A9 phosphate, a Mg^{2+} ion, and four nearby waters (three of which are directly coordinating Mg^{2+}). The remainder of the system was treated with the molecular mechanical force field, described above.

The minimum free energy paths were determined by repeating finite temperature string umbrella sampling simulations using different sets of reaction coordinates in successively higher dimensions. For 3D surfaces, the mechanism was described by 3 bond length differences that track the progress of the general base ($\xi_{GB} = R_{O2'-H} - R_{G12:N1-H}$), phosphoryl transfer ($\xi_{PT} = R_{O5'-P} - R_{O2'-P}$), and general acid ($\xi_{GA} = R_{G8:O2'-H} - R_{O5'-H}$) steps (Figure 2). For the 4D surface, a separate set of umbrella window simulations were carried out to explicitly track the O2′-P and O5′-P bond distances rather than the combined coordinate ξ_{PT} used to monitor the phosphoryl transfer. In other words, the four reaction coordinates are ξ_{GB}, $R_{O2'-P}$, $R_{O5'-P}$, and ξ_{GA}. A 6D profile was similarly constructed by decomposing the combined ξ_{GB} and ξ_{GA} coordinates into their component distances as well. The umbrella window locations were iteratively refined to converge upon the minimum free energy path using the string method described in ref 98. This method

https://doi.org/10.1021/acs.jpca.1c00736
J. Phys. Chem. A 2021, 125, 4216−4232

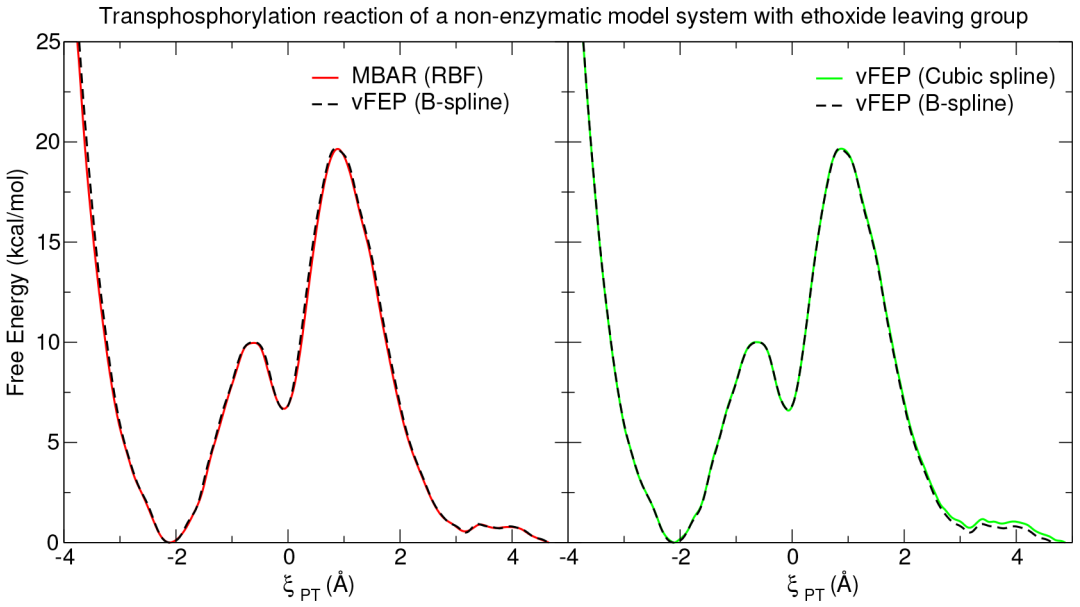

Figure 3. Free energy curve (1D) for the associative transphosphorylation reaction of a nonenzymatic model system with an ethoxide leaving group (illustrated in Figure 1) simulated with PBE0/6-31G* QM/MM in explicit TIP4P/Ew water. Analysis with vFEP (B-spline) was carried out using B-spline order 5 and 0.15 Å node spacing.

combines the finite temperature string method[66] with umbrella sampling simulations,[37] and it has sometimes been referred to as the finite-temperature string umbrella sampling method.[99] In brief, an initial guess is made for a parametric curve that defines the reaction pathway. Umbrella window molecular dynamics simulations are carried out along the parametric curve by uniformly discretizing the path. The parametric curve is then updated by fitting it to the observed average reaction coordinate values from each simulation. In the present work, the parametric curve is obtained by Akima spline discretized with 32 umbrella window simulations, and the iterative process is repeated 50 times. A 100 kcal/mol force constant was used for each reaction coordinate in all umbrella simulations. Each umbrella window simulation was run for 2 ps. The reported free energy pathway is the parametric curve generated by the last iteration, and the free energy values are obtained by analyzing the data from all 50 iterations.

RESULTS AND DISCUSSION

We implemented a free energy analysis program, available for download on the internet,[69] that enables the use of MBAR and vFEP for FESs of any dimension. The results discussed in this section include a comparison of these methods for 1D, 2D, and 3D FESs. We also compare the results obtained from a previously published vFEP method based cubic splines; however, that program is limited to 1D and 2D FESs only. Furthermore, we explore the sensitivity of the FESs with respect to grid spacing, cardinal B-spline order, umbrella window spacing, and their computational cost. Finally, we examine how 1D projections of minimum free energy paths vary with respect to the dimensionality of the calculated FES.

1D Example: Nonenzymatic Transphosphorylation Reaction in Solution. The purpose of this section is to concisely demonstrate that for a simple 1D example there is consistency between vFEP methods using cubic spline and B-spline representations of the data and that these FESs are also consistent with MBAR results. The 1D FES of a model transphosphorylation reaction (Figure 1) simulated with an *ab initio* QM/MM method is shown in Figure 3. The cardinal B-spline solution uses fifth-order B-splines and a 0.15 Å node spacing. The MBAR histogram spacing is 0.15 Å, and the 1D FESs connects the MBAR histogram values using RBFs. The cubic spline vFEP method is described in ref 52. The MBAR, cardinal B-spline vFEP, and cubic spline vFEP methods are all nearly indistinguishable from each other. Furthermore, each method requires only a fraction of a second to compute the FES. The rate limiting barriers (kcal/mol) are 19.65 (MBAR), 19.67 (B-spline vFEP), and 19.67 (cubic spline vFEP). Hence, for the 1D example, all methods provide very consistent and affordable results.

2D Example: ϕ/ψ (Ramachandran) Conformational Maps for Dipeptides in Solution. The purpose of this section is to illustrate that the vFEP B-spline method is of equivalent or superior accuracy and computational efficiency for 2D applications to the vFEP cubic spline implementation and that both vFEP methods perform better than MBAR using a numerical histogram data representation. The 2D Ramachandran FESs of glycine, alanine, and valine dipeptide are shown in Figure 4.

The cardinal B-spline FESs use fifth-order B-splines and a 10° node spacing. The MBAR histogram spacing is 10°. The colored blocks in the MBAR FES are the histogram free energy values, whereas the stationary points and minimum energy path are determined from a B-spline representation of the histogram values. The free energy pathways were obtained from minimizations on the reduced dimensional FES rather than explicit dynamical simulation of the physical system. The procedure is analogous to our description of the finite temperature string umbrella sampling method; however, minimizations are carried out on the umbrella-biased FES rather than performing umbrella simulations. In this sense, one can consider the procedure to be a zero-temperature string umbrella minimization method. The peptide dihedral angles are periodic coordinates; therefore, the positions of the

https://doi.org/10.1021/acs.jpca.1c00736
J. Phys. Chem. A 2021, 125, 4216−4232

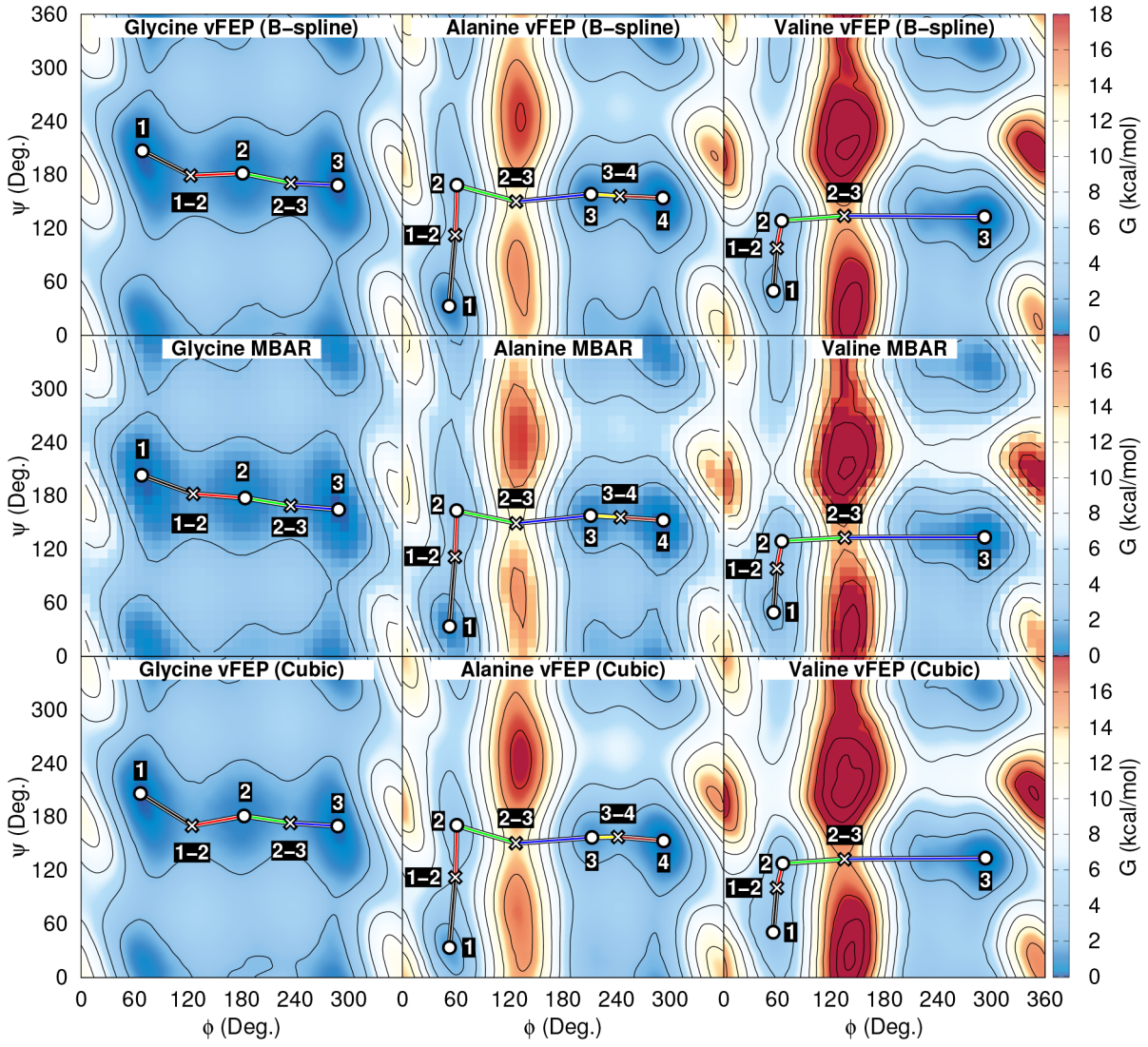

Figure 4. Glycine, alanine, and valine dipeptide FESs analyzed with vFEP and MBAR. The ϕ and ψ coordinates are the peptide dihedral angles. The umbrella window spacing is 8° in each dimension. Analysis with vFEP (B-spline) was carried out using B-spline order 5 and 10° node spacing.

observed reaction coordinates are treated with a minimum image convention. The cardinal B-spline vFEP method does not require a buffer region to define the free energy within the periodic range. Instead, evaluation of the FES near the boundary make use of the B-spline node parameters that wrap to the other side of the periodic range. Similarly, the cubic spline vFEP method[52] must vary the spline coefficients with consideration of the periodic boundary conditions.

We selected 3 or 4 minima from each system, connected them by a minimum energy path, and tabulated the stationary point positions and FES values in Table 1. In summary, the mean difference in the stationary point locations between B-spline vFEP and MBAR are 3.7, 1.5, and 0.7° for glycine, alanine, and valine, respectively. The larger differences in the glycine FES appear to be related to the broad, shallow minima. The root-mean-square deviation between the B-spline vFEP and MBAR stationary point FES values are less than 0.08 kcal/mol for each system. The cubic spline vFEP method does not compare as well to the MBAR results; the mean difference in locations are 5.8, 2.2, and 1.4° for glycine, alanine and valine, respectively, and the root-mean-square deviation between the cubic spline vFEP and MBAR FES values are 0.16, 0.57, and 0.68 kcal/mol.

Figure 5 illustrates the sensitivity of the glycine minimum energy path with respect to grid spacing and cardinal B-spline order. The grid spacing does not effect the number of umbrella window simulations being analyzed, but it does effect the number of optimizable B-spline parameters. As the grid spacing decreases, the number of optimizable parameters increase and the B-splines are more capable of capturing the numerical noise in the data by introducing polynomic oscillations. The MBAR method suffers from a similar phenomenon whereby numerical noise becomes more pronounced when the histogram bin sizes are small. Figure 5 also shows the glycine minimum energy path is not sensitive to the cardinal B-spline order. Order 3 B-splines are the smallest order that produce smooth curves. Order 1 B-splines are discontinuous offset constants, and order 2 B-splines linearly interpolate between the nearest corners.

The nonenzymatic transphosphorylation reaction and Ramachandran profiles are expected to yield smooth FESs due to their simplicity; however, it may be difficult to

https://doi.org/10.1021/acs.jpca.1c00736
J. Phys. Chem. A 2021, 125, 4216−4232

Table 1. Selected Stationary Points from the Glycine, Alanine, and Valine Dipeptide FESs Shown in Figure 4

	vFEP (B-spline)			MBAR (B-spline)			vFEP (Cubic)		
label	ϕ (deg)	Ψ (deg)	ΔG (kcal/mol)	ϕ (deg)	ψ (deg)	ΔG (kcal/mol)	ϕ (deg)	ψ (deg)	ΔG (kcal/mol)
					Glycine				
(**1**)	68.9	206.8	0.03	67.9	203.1	0.05	66.6	206.3	−0.05
(**1**−**2**)	122.7	179.1	1.65	125.8	182.2	1.58	124.3	170.2	1.44
(**2**)	181.0	181.7	0.60	183.8	177.6	0.54	182.7	181.1	0.80
(**2**−**3**)	235.1	170.7	1.69	235.0	169.0	1.64	234.5	173.3	1.83
(**3**)	287.8	168.2	0.00	288.7	164.6	0.00	287.8	169.8	0.00
					Alanine				
(**1**)	52.4	32.7	0.81	52.9	33.6	0.73	52.8	33.6	1.42
(**1**−**2**)	59.2	112.3	4.45	58.9	111.6	4.37	59.2	112.3	5.08
(**2**)	61.0	168.4	2.76	60.7	163.5	2.75	60.9	170.8	3.37
(**2**−**3**)	127.4	150.0	13.20	127.5	149.3	13.06	127.1	150.6	13.69
(**3**)	211.3	158.3	0.88	210.8	157.9	0.81	212.3	157.0	1.40
(**3**−**4**)	243.7	156.1	1.63	244.5	155.9	1.57	241.5	157.6	1.95
(**4**)	291.9	154.0	0.00	292.3	152.6	0.00	292.7	153.2	0.00
					Valine				
(**1**)	55.6	49.9	1.92	55.9	49.4	1.98	55.4	50.7	2.80
(**1**−**2**)	59.4	98.0	2.80	59.5	98.5	2.88	59.7	100.5	3.67
(**2**)	65.0	128.5	2.46	65.1	129.2	2.59	66.1	127.9	3.45
(**2**−**3**)	135.1	134.0	14.56	135.6	133.2	14.62	135.4	132.6	15.14
(**3**)	292.2	133.0	0.00	292.3	133.5	0.00	293.4	133.9	0.00

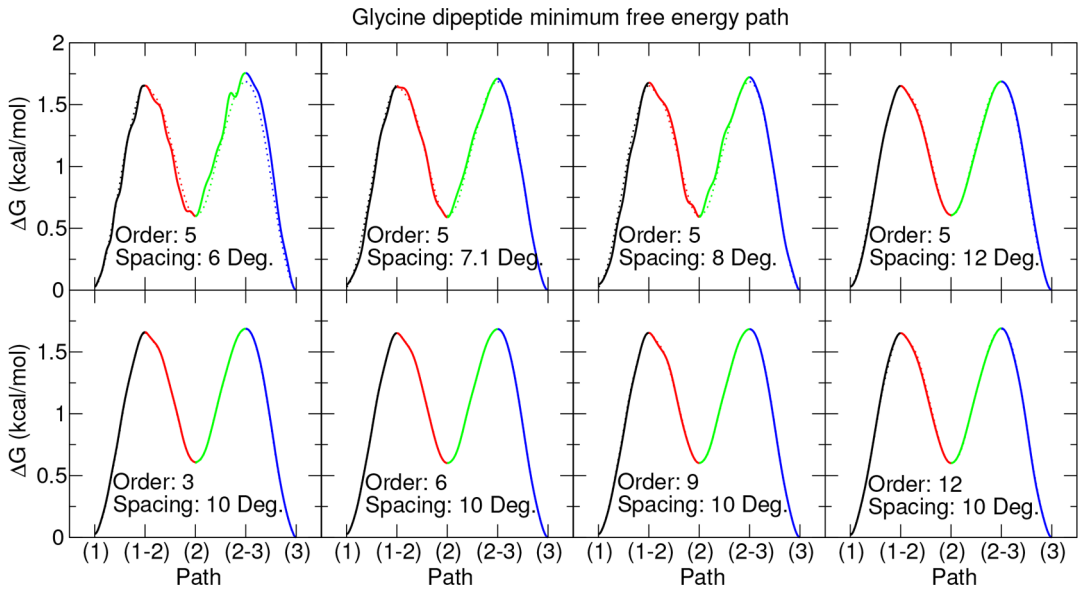

Figure 5. Comparison of vFEP glycine dipeptide minimum free energy paths as a function of cardinal B-spline order and node spacing. The stationary points labels correspond to those shown in Figure 4. The dotted line in each pane is the vFEP result using fifth-order B-splines and a 10° node spacing.

distinguish between numerical noise and physically relevant features in FESs of highly diffusive processes such as those which might appear in protein conformational changes and protein folding. One approach explored in previous work to deal with numerical noise is to use Gaussian process regression to *fit* a smooth function to binned free energy values contaminated with numerical noise.[51] The approach used in the present work is to choose a sufficiently large bin width to reduce the numerical noise and then *interpolate* between the observed values. In the context of MBAR, the histogram bins effectively average the free energy in a their respective regions of space, thus eliminating features within their interior. The free energy at the bin center is assumed to be the average value, and values near the histogram edges are approximated by interpolation. The strategy is to choose a small bin width to reduce the errors in these approximations, but large enough for each bin to contain a sufficient number of samples to adequately model the probability density. If the bins become too small, then the FES will contain noise and possibly artificial minima. For example, Figure 6a plots the number of minima on the nonenzymatic transphosphorylation reaction profile as a function of MBAR histogram bin width. The number of minima stabilizes for widths larger than 0.1 Å. This does not mean that the FESs using widths near 0.1 Å are free of numerical noise; it only means that the magnitude of the noise is not large enough to produce additional minima. The

https://doi.org/10.1021/acs.jpca.1c00736
J. Phys. Chem. A 2021, 125, 4216−4232

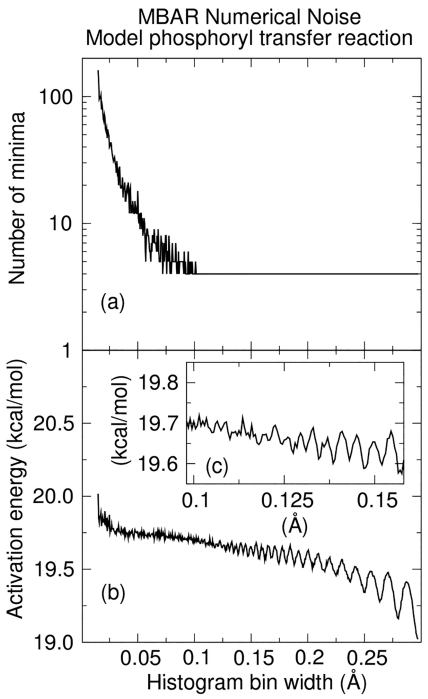

Figure 6. (a) Number of minima in the 1D nonenzymatic transphosphorylation reaction computed with MBAR and interpolated with RBFs. The image shows how the number of minima change as the histogram bin width is varied. (b) Activation free energy as a function of histogram bin width. The reactant and transition state free energies are the lowest and highest free energies found in the region of the reactant well and transition state region, respectively. (c) Zoomed version of (b) in the range of 0.10−0.15 Å bin width.

addition of noise will also effect the activation energy (the difference between the lowest free energy near the reactant minimum and the highest free energy near the transition state), as shown in Figure 6b. As the noise increases, the gap between these limits will also increase. Alternately, if the bin widths become large, then the binning of data may result in an underestimation of the transition state free energies and overestimation of the free energies near the minima. Figure 6c plots the activation energy for bin widths between 0.1 Å (which is the smallest width that yields a stable number of minima) and 0.15 Å. In this range, the activation energy ranges from 19.6 to 19.7 kcal/mol. Ultimately, the inspection of Figure 6b is not a very good approach for choosing bin widths because it compares two points on the surface to make a judgment on the entire surface. We find Figure 6a to be a better means for distinguishing between noise and real features in simple surfaces. For complicated systems, a general mechanism for properly distinguishing numerical noise from real features may require multiple, independent umbrella window simulations.

Figure 7 compares the MBAR and vFEP wallclock times as a function of the number of windows included in the 2D analysis of the alanine dipeptide system. To make this plot, entire rows or columns from the 2D matrix of umbrella windows were uniformly deleted to create a sparse set of data to compare timings. For the vFEP methods, the timings include the nonlinear optimization of eq 2. The MBAR timings include the optimization of eq 23 and the evaluation of eq 20. The B-spline and cubic spline vFEP methods scale linearly with respect to the number of umbrella windows. The MBAR method scales quadratically. The quadratic character of the MBAR timings is more easily seen by comparing the ratio of timings between MBAR and B-spline vFEP, which scales linearly. The cardinal B-spline vFEP method is the fastest of the three. When the full set of data is analyzed, the B-spline vFEP method is 42 times faster than the cubic spline vFEP method and 166 times faster than MBAR. Optimization of the MBAR/UWHAM objective function using the full set of simulation data required 12 h on a single Intel Xeon E5−2630 v3 (2.60 GHz) core, whereas the optimization of the vFEP B-spline parameters was completed within 5 min.

Figure 8 illustrates the behavior of the vFEP and MBAR FESs of alanine dipeptide as the number of umbrella window simulations included in the analysis becomes sparse. As the umbrella window spacing increases, fewer simulations are included in the analysis. The regular grid spacing of B-spline

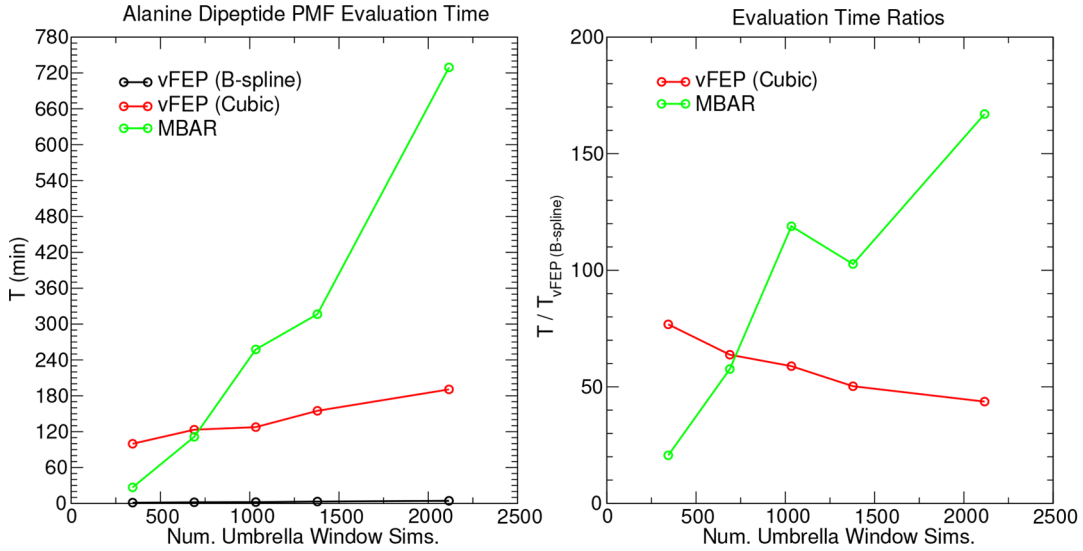

Figure 7. Wallclock time required to optimize the vFEP (eq 2) and MBAR/UWHAM (eqs 20 and 23) objective functions for the 2D alanine dipeptide FES as a function of the number of umbrella window simulations. Each simulation contributes 2000 data points.

https://doi.org/10.1021/acs.jpca.1c00736
J. Phys. Chem. A 2021, 125, 4216−4232

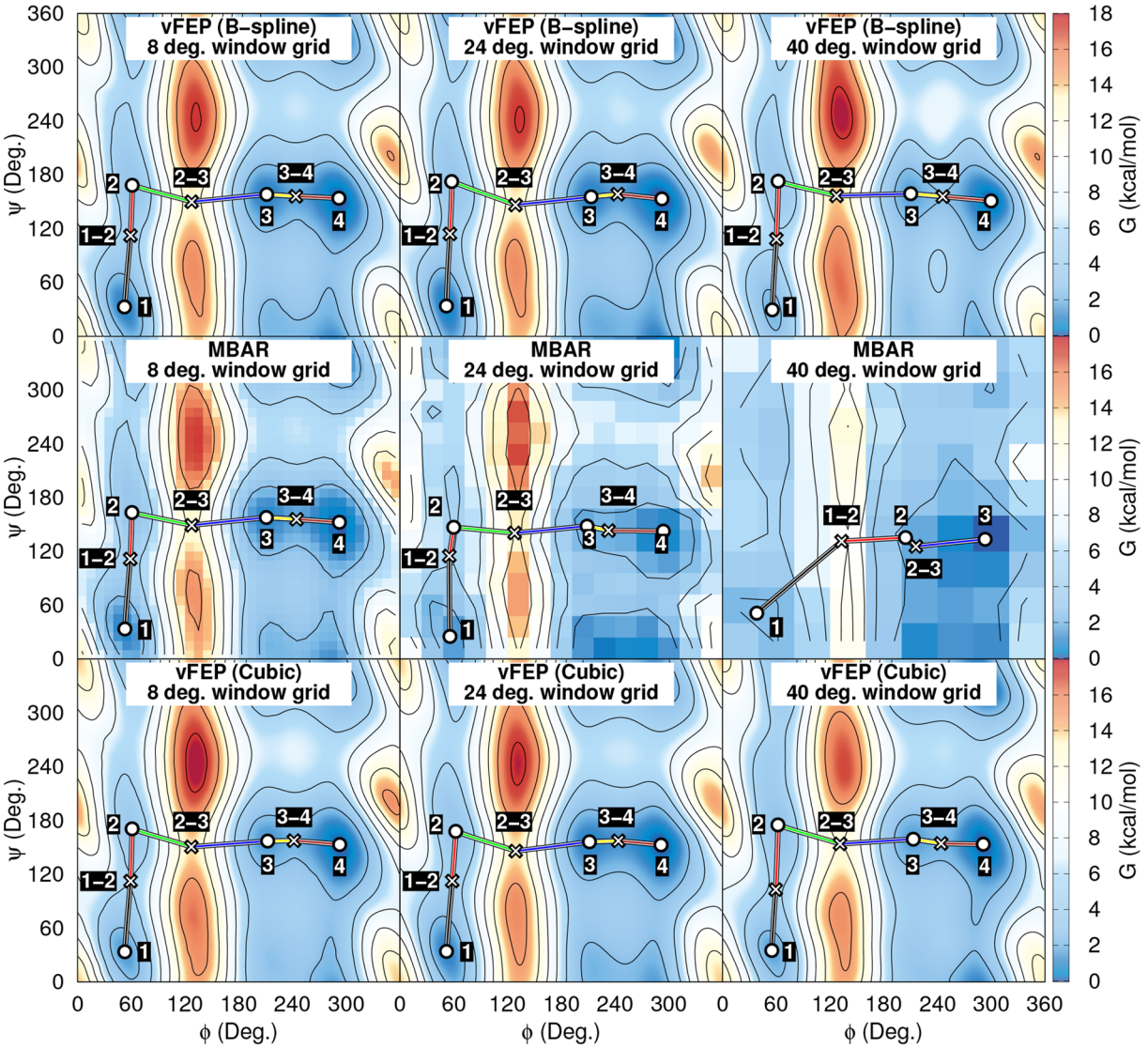

Figure 8. Alanine dipeptide FESs analyzed with vFEP and MBAR. The ϕ and ψ coordinates are the peptide dihedral angles. The umbrella window spacing are 8, 24, and 40° in the left, center, and right columns, respectively.

control points increases from 10° to 24 and 40° as the regular grid of umbrella windows increases from 8° to 24 and 40°, respectively. The regular grid spacing of MBAR histogram bins and the cubic spline vFEP control points are similarly increased. By increasing the width of the histogram bins (or separation between control points), we avoid encountering spatial gaps in the observed samples when the number of simulations becomes sparse. The blocks of solid colors in the MBAR FESs are the histogram free energy values; however, the free energy pathway and stationary point locations are determined from B-spline interpolation through the histogram values. The cubic spline and cardinal B-spline vFEP methods produce nearly indistinguishable surfaces using 8 and 24° umbrella window spacing. When the spacing is increased to 40°, the vFEP methods still appear to be qualitatively correct. In contrast, the quality of the MBAR surface degrades as the spacing is increased. At a 40° spacing, the MBAR method fails to predict one of the minima and associated transition state. The observation that vFEP yields good quality FESs with sparse umbrella window data is consistent with previous work.[52,53]

3D, 4D, and 6D Examples: Enzymatic Transphosphorylation Reaction Catalyzed by HHr. Previous formulations of vFEP could only be applied to 1D and 2D FESs;[52,53] therefore, the purpose of this section is to apply the B-spline vFEP and MBAR methods to the calculation of a 3D FES. We have chosen a well studied archetype RNA enzyme, using HHr for the example.[88,100−103] Study of HHr, along with other small self-cleaving ribozymes,[104] has provided new insight into RNA enzyme design.[61] HHr catalyzes the self-cleavage of the RNA phosphodiester backbone using a general acid−base mechanism[60] illustrated in Figure 2. The reaction involves activation of a 2′OH nucleophile by a general base guanine residue (deprotonated at the N1 position). The resulting 2′O oxyanion then makes an in-line attack to the adjacent scissile phosphate to form a pentavalent dianionic transition state (or high-energy intermediate), followed by departure of the O5′ leaving group with the assistance of a proton that is donated from a general acid. Hence, there are three fundamental reaction coordinates used to represent progression of the general base ($\xi_{GB} = R_{O2'-H} - R_{G12:N1-H}$), phosphoryl transfer

https://doi.org/10.1021/acs.jpca.1c00736
J. Phys. Chem. A 2021, 125, 4216−4232

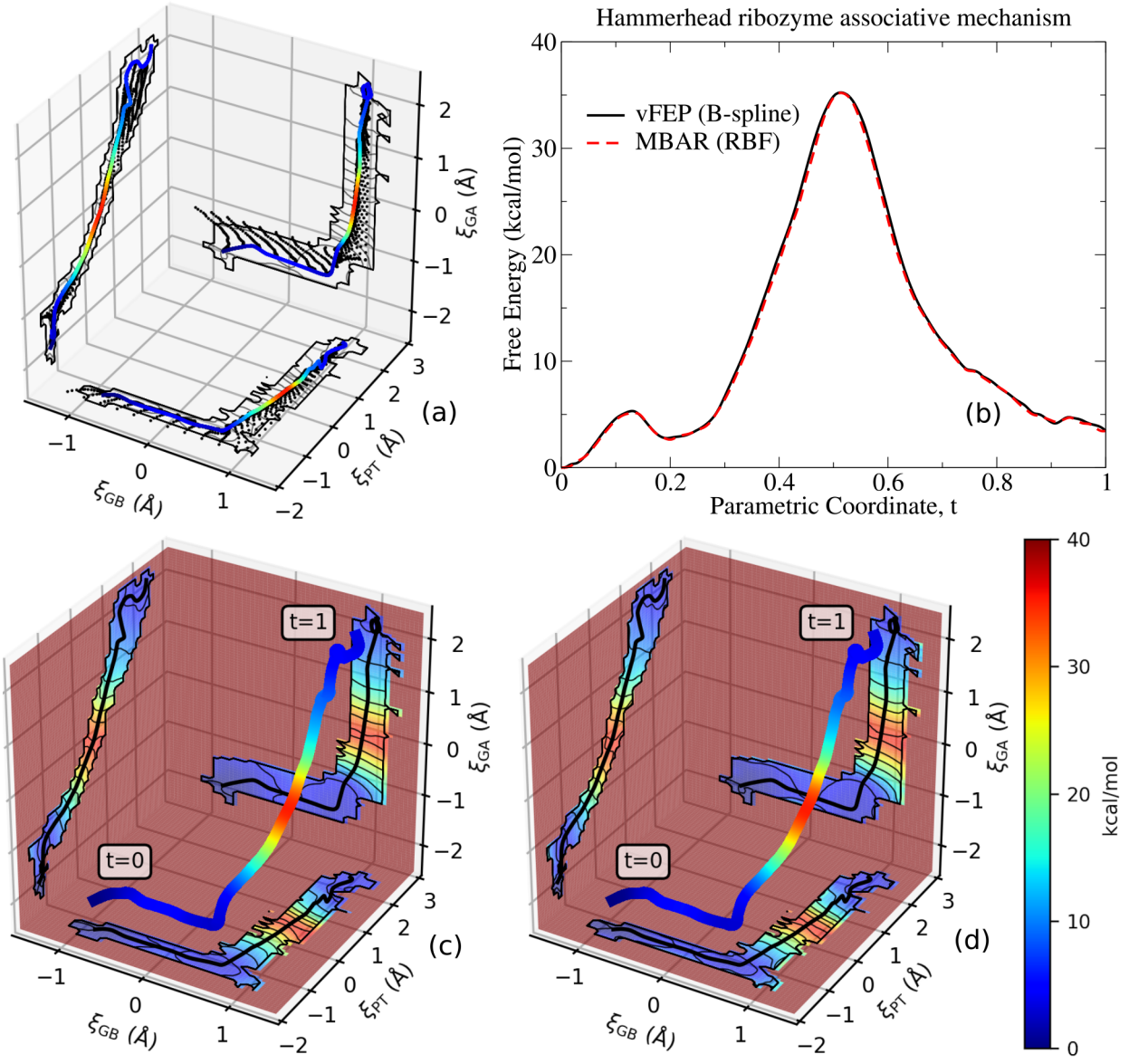

Figure 9. Free energy surface (3D) for the associative transphosphoylation reaction catalyzed by the HHr (illustrated in Figure 2) computed from AM1/d-PhoT QM/MM. Subplot (a) shows the umbrella window locations encountered by the finite temperature string umbrella sampling method. The umbrella window locations are projected onto planes intersecting the final path, which is shown as the colored line. The RBF MBAR and B-spline vFEP free energy profile of the final path is shown in (b). (c and d) RBF MBAR and B-spline vFEP free energy surfaces projected onto planes that intersect the final path.

($\xi_{PT} = R_{O5'-P} - R_{O2'-P}$), and general acid ($\xi_{GA} = R_{G8:O2'-H} - R_{O5'-H}$) steps (Figure 2).

Figure 9 illustrates the 3D FESs of the associative transphosphorylation reaction pathway catalyzed by the HHr computed using AM1/d-PhoT[97] QM/MM. The MBAR and cardinal B-spline vFEP method yield near identical results. The B-spline vFEP reaction barrier is 35.24 kcal/mol, which closely agrees with the MBAR value of 35.20 kcal/mol. The comparison of analysis times is shown in Figure 10. When all 50 string iterations are included in the analysis, the MBAR method is 4.5 times faster than the B-spline vFEP method. When fewer string iterations are included, the MBAR method is 10−20 times faster. The vFEP method becomes more competitive as the number of simulations increase because the B-spline vFEP and MBAR methods scale linearly and quadratically with respect to the number of simulations, respectively. Relative to the 2D timings, the performance of the MBAR and B-spline vFEP methods are far more comparable to each other for 3D analysis because the scaling of the MBAR method does not depend on dimensionality, whereas the numerical integration of the vFEP configuration integral quickly increases as the dimensionality increases. On the basis of the formal scaling of the algorithms and the observed timings of 2D and 3D analysis, we conclude that the MBAR approach is more practical for analyzing FESs involving four or more reaction coordinates, and thus we use this approach in the 4D and 6D examples below.

Calculated reaction pathways and barrier heights are effected by restricting the free energy profile to a reduced hypersurface of reaction coordinates. Performing the analysis with limited

https://doi.org/10.1021/acs.jpca.1c00736
J. Phys. Chem. A 2021, 125, 4216−4232

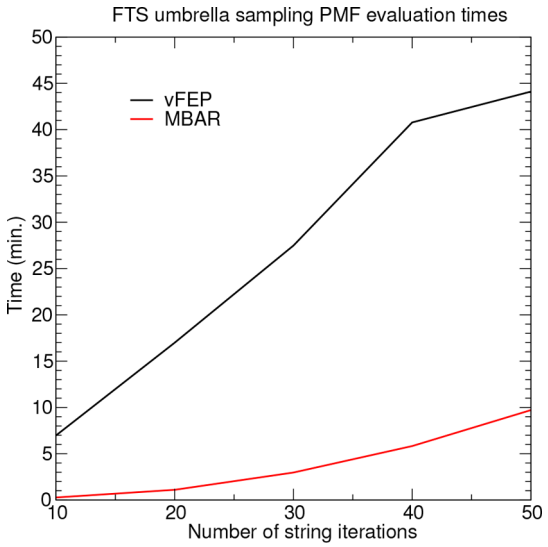

Figure 10. Comparison of evaluation times for generating the 3D hammerhead ribozyme FES as a function of the number of finite temperature string umbrella sampling iterations. Each iteration contributes 32 umbrella window simulations, and each umbrella window simulation contributes 80 data points.

degrees of freedom effectively imposes constraints on the free energy. The remainder of this section illustrates application of the MBAR method for analyzing 3D, 4D, and 6D FESs from the finite-temperature string umbrella sampling method. Comparison of 3D, 4D, and 6D FESs enable one to explore the degree to which the pathway and barriers are affected by choice of reaction coordinates. The 3D surface of the associative reaction consisted of ξ_{GB}, ξ_{PT}, and ξ_{GA} coordinates. Each of these coordinates are bond length differences between 3 atoms. We constructed a 4D profile by explicitly tracking the O2′−P and O5′−P bond distances, rather than the combined coordinate ξ_{PT}, to describe the phosphoryl transfer coordinate. In other words, the four reaction coordinates are ξ_{GB}, $R_{O2'-P}$, $R_{O5'-P}$, and ξ_{GA}. Exploration of these degrees of freedom separately can help to identify and distinguish associative pathways where nucleophilic attack occurs first versus dissociative pathways where leaving group departure occurs first. A 6D profile was similarly constructed by decomposing the combined ξ_{GB} and ξ_{GA} coordinates into their component distances as well. The minimum free energy path was searched in the space of 3D, 4D, and 6D reaction coordinates, and the MBAR free energies along the converged pathways are shown in Figure 11. The free energy barriers and average distances in the transition state ensemble are summarized in Table 2. The umbrella window simulations used to characterize the 3D, 4D, and 6D profiles were carried out independently; that is, the 4D and 6D profiles are not a reanalysis of the umbrella window simulations generated for the 3D profile. Overall, the profiles are qualitatively similar (Figure 11a); however, the 4D and 6D reaction barriers are 0.6 and 1.5 kcal/mol lower than the 3D barrier, respectively. This is consistent with the added degrees of freedom that enable identification of a slightly lower free energy pathway. Figure 11b shows that the 6D profile yields an "earlier" transition state (larger degree or O2′−P bond formation and smaller degree of O5′−P bond cleavage) than the 3D or 4D profiles. The comparison of transition state bond lengths suggests that the largest difference in the 6D profile is the O5′−P distance which undergoes a systematic contraction as the degrees of freedom increase. This contraction of the O5′−P distance is coupled with an increase in the O5′−H distance. This implies that cleavage of the O5′−P bond is less advanced, as is the degree of proton transfer (O5′−H bond formation) from the general acid. While this is a fairly subtle difference, it is nonetheless significant and could be detected experimentally by measurement of linear free energy relations[105,106] or kinetic isotope effects[107,108] at primary and secondary oxygen positions, similar to those carried out recently for similar reactions in the Varkud satellite ribozyme[56] and RNase A.[109,110]

Hence, the ability to analyze and construct robust multidimensional free energy surfaces is important for mechanistic studies of protein and RNA enzymes. Frequently, 2D or 3D surfaces are used with fairly dense sampling and coverage throughout the coordinate space in order to identify the main reaction pathways in a reduced coordinate space. These pathways can then undergo refinement to provide further resolution. The methods presented in the present work provide powerful analysis tools for construction of robust analytic FESs for both of these scenarios. It is the hope that the

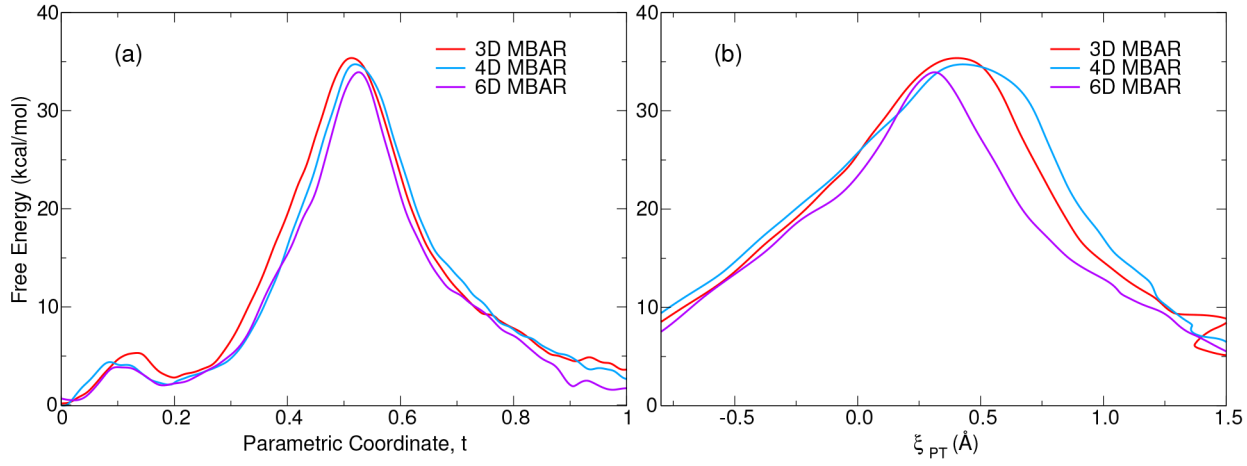

Figure 11. Comparison of minimum free energy paths from 3D, 4D, and 6D representations of the associative transphosphoylation reaction catalyzed by the HHr. Left panel: RBF MBAR free energy with respect to progress along the path. Right panel: MBAR results with respect to the phosphoryl transfer coordinate ξ_{PT}.

https://doi.org/10.1021/acs.jpca.1c00736
J. Phys. Chem. A 2021, 125, 4216−4232

Table 2. Free Energy Barrier (kcal/mol) and Average Distances (Å) from the 3D, 4D, and 6D Minimum Free Energy Pathways of the Associative Transphosphoylation Reaction Catalyzed by HHr[a]

	$\Delta G^{\ddagger}$	G12:N1−H	O2′−H	O2′−P	O5′−P	O5′−H	G8:O2′−H
3D	35.2	1.03	1.89	1.82	2.27	1.35	1.24
4D	34.6	1.03	1.89	1.79	2.22	1.38	1.20
6D	33.8	1.02	1.88	1.83	2.06	1.41	1.20

[a]Atom labels are defined in Figure 2.

use of these tools which have been implemented in the FE-ToolKit software package[69] will enable new insights to be gained and facilitate discovery for a wide array of free energy applications.

CONCLUSIONS

We implemented two strategies for calculating high-dimensional FES profiles. We provided examples that utilized the methods to analyze 1D, 2D, 3D, 4D, and 6D FESs. The first strategy that we implemented is based on the vFEP method. Previous implementations of vFEP used a cubic spline function to parametrize the FES; however, the software was limited to 1D and 2D FES analysis. Our implementation uses cardinal B-spline functions to parametrize the FES. This functional form allowed us to extend the implementation to arbitrary dimensions and improve the efficiency of vFEP by exploiting the B-spline's compact support. Our B-spline vFEP method was shown to be 50 times faster than a previous implementation of cubic spline vFEP when applied to the analysis of 2D Ramachandran profiles. The second strategy that we implemented used the MBAR method to generate an unbiased probability density from a global reweighting of the observed samples. The principles behind the MBAR approach are not new to this manuscript; however, we note the following: (1) Our implementation makes use of the fast MBAR/UWHAM method for generating FESs, rather than solving the coupled MBAR equations. (2) We made the use of MBAR FESs practical for high dimensions. (3) We introduced the use of B-splines and multiquadric radial basis functions to interpolate between the histogram FES values. We demonstrated that the cardinal B-spline and MBAR FESs produce nearly identical 1D, 2D, and 3D FES profiles. We compared the performance between the vFEP and MBAR methods and found that the B-spline vFEP method is 150 times faster than MBAR when applied to periodic 2D FESs but that the MBAR method is 4.5 times faster than vFEP when evaluating unbounded 3D profiles. In other words, both methods are useful, but they appear to offer different performance advantages depending on the situation. In addition to vFEP being much faster at computing 2D FESs, we also demonstrated that the vFEP method produced FESs of superior quality when the surface was only sparsely sampled. The associative mechanism of Hammerhead ribozyme was examined using 3D, 4D, and 6D profiles, and it was found that the 4D and 6D reaction barriers were 0.6 and 1.5 kcal/mol smaller than 3D profiles. This work has thus developed and demonstrated new B-spline vFEP and MBAR methods for creation and analysis of robust, analytic free energy surfaces in arbitrary dimensions, and provided the broad scientific community with new software tools in FE-ToolKit that will enable their application to important problems.

AUTHOR INFORMATION

Corresponding Author

Darrin M. York − *Laboratory for Biomolecular Simulation Research, Institute for Quantitative Biomedicine and Department of Chemistry and Chemical Biology, Rutgers University, Piscataway, New Jersey 08854-8087, United States;* orcid.org/0000-0002-9193-7055; Email: Darrin.York@rutgers.edu

Authors

Timothy J. Giese − *Laboratory for Biomolecular Simulation Research, Institute for Quantitative Biomedicine and Department of Chemistry and Chemical Biology, Rutgers University, Piscataway, New Jersey 08854-8087, United States*

Şölen Ekesan − *Laboratory for Biomolecular Simulation Research, Institute for Quantitative Biomedicine and Department of Chemistry and Chemical Biology, Rutgers University, Piscataway, New Jersey 08854-8087, United States;* orcid.org/0000-0002-5598-5754

Complete contact information is available at: https://pubs.acs.org/10.1021/acs.jpca.1c00736

Notes

The authors declare no competing financial interest.

ACKNOWLEDGMENTS

The authors are grateful for financial support provided by the National Institutes of Health (nos. GM107485 and GM062248). Computational resources were provided by the National Institutes of Health under grant no. S10OD012346, the Office of Advanced Research Computing (OARC) at Rutgers, the State University of New Jersey, and by the Extreme Science and Engineering Discovery Environment (XSEDE),[111] specifically the resources COMET and COMET GPU, which is supported by National Science Foundation grant no. ACI-1548562 (allocation number TG-CHE190067). The authors also acknowledge the Texas Advanced Computing Center (TACC, http://www.tacc.utexas.edu) at The University of Texas at Austin for providing HPC resources, specifically the Frontera Supercomputer, that have contributed to the research results reported within this paper.

REFERENCES

(1) Jorgensen, W. L. Free energy calculations: a breakthrough for modeling organic chemistry in solution. *Acc. Chem. Res.* **1989**, *22*, 184−189.

(2) Straatsma, T. P.; McCammon, J. A. Computational alchemy. *Annu. Rev. Phys. Chem.* **1992**, *43*, 407−435.

(3) Chipot, C., Pohorille, A., Eds. *Free Energy Calculations: Theory and Applications in Chemistry and Biology*; Springer Series in Chemical Physics; Springer: New York, 2007; Vol. *86*.

(4) Lee, T.-S.; Allen, B. K.; Giese, T. J.; Guo, Z.; Li, P.; Lin, C.; McGee, T. D., Jr.; Pearlman, D. A.; Radak, B. K.; Tao, Y.; et al.

Alchemical Binding Free Energy Calculations in AMBER20: Advances and Best Practices for Drug Discovery. *J. Chem. Inf. Model.* **2020**, *60*, 5595−5623.
(5) Elber, R.; Karplus, M. A method for determining reaction paths in large molecules: Apllication to myoglobin. *Chem. Phys. Lett.* **1987**, *139*, 375−380.
(6) Fischer, S.; Karplus, M. Conjugate Peak Refinement: An Algorithm For Finding Reaction Paths And Accurate Transition States In Systems With Many Degrees Of Freedom. *Chem. Phys. Lett.* **1992**, *194*, 252−261.
(7) Grubmüller, H. Predicting slow structural transitions in macromolecular systems: Conformational flooding. *Phys. Rev. E: Stat. Phys., Plasmas, Fluids, Relat. Interdiscip. Top.* **1995**, *52*, 2893−2906.
(8) Yang, A.-S.; Honig, B. Free energy determinants of secondary structure formation: II. antiparallel β-sheets. *J. Mol. Biol.* **1995**, *252*, 366−376.
(9) Simmerling, C.; Fox, T.; Kollman, P. A. Use of Locally Enhanced Sampling in Free Energy Calculations: Testing and Application to the $\alpha \rightarrow \beta$ Anomerization of Glucose. *J. Am. Chem. Soc.* **1998**, *120*, 5771−5782.
(10) Apostolakis, J.; Ferrara, P.; Caflisch, A. Calculation of conformational transitions and barriers in solvated systems: Application to the alanine dipeptide in water. *J. Chem. Phys.* **1999**, *110*, 2099−2108.
(11) Garate, J. A.; Oostenbrink, C. Free-energy differences between states with different conformational ensembles. *J. Comput. Chem.* **2013**, *34*, 1398−1408.
(12) Turupcu, A.; Oostenbrink, C. Modeling of Oligosaccharides within Glycoproteins from Free-Energy Landscapes. *J. Chem. Inf. Model.* **2017**, *57*, 2222−2236.
(13) Bash, P. A.; Singh, U. C.; Brown, F. K.; Langridge, R.; Kollman, P. A. Calculation of the relative change in binding free energy of a protein-inhibitor complex. *Science* **1987**, *235*, 574−576.
(14) Hwang, J.-K.; Warshel, A. Semiquantitative Calculations of Catalytic Free Energies in Genetically Modified Enzymes. *Biochemistry* **1987**, *26*, 2669−2673.
(15) Kottalam, J.; Case, D. A. Dynamics of Ligand Escape from the Heme Pocket of Myoglobin. *J. Am. Chem. Soc.* **1988**, *110*, 7690−7697.
(16) He, X.; Liu, S.; Lee, T.-S.; Ji, B.; Man, V. H.; York, D. M.; Wang, J. Fast, Accurate, and Reliable Protocols for Routine Calculations of Protein-Ligand Binding Affinities in Drug Design Projects Using AMBER GPU-TI with ff14SB/GAFF. *ACS Omega* **2020**, *5*, 4611−4619.
(17) Miao, Y.; Bhattarai, A.; Wang, J. Ligand Gaussian accelerated molecular dynamics (LiGaMD): Characterization of ligand binding thermodynamics and kinetics. *J. Chem. Theory Comput.* **2020**, *16*, 5526−5547.
(18) Cruz, J.; Wickstrom, L.; Yang, D.; Gallicchio, E.; Deng, N. Combining Alchemical Transformation with a Physical Pathway to Accelerate Absolute Binding Free Energy Calculations of Charged Ligands to Enclosed Binding Sites. *J. Chem. Theory Comput.* **2020**, *16*, 2803−2813.
(19) Cui, D.; Zhang, B. W.; Tan, Z.; Levy, R. M. Ligand Binding Thermodynamic Cycles: Hysteresis, the Locally Weighted Histogram Analysis Method, and the Overlapping States Matrix. *J. Chem. Theory Comput.* **2020**, *16*, 67−79.
(20) Perthold, J. W.; Petrov, D.; Oostenbrink, C. Toward Automated Free Energy Calculation with Accelerated Enveloping Distribution Sampling (A-EDS). *J. Chem. Inf. Model.* **2020**, *60*, 5395−5406.
(21) Sakae, Y.; Zhang, B. W.; Levy, R. M.; Deng, N. Absolute Protein Binding Free Energy Simulations for Ligands with Multiple Poses, a Thermodynamic Path That Avoids Exhaustive Enumeration of the Poses. *J. Comput. Chem.* **2020**, *41*, 56−68.
(22) Homeyer, N.; Gohlke, H. Extension of the free energy work flow FEW towards implicit solvent/implicit membrane MM-PBSA calculations. *Biochim. Biophys. Acta, Gen. Subj.* **2015**, *1850*, 972−982.
(23) Gumbart, J. C.; Teo, I.; Roux, B.; Schulten, K. Reconciling the Roles of Kinetic and Thermodynamic Factors in Membrane Protein Insertion. *J. Am. Chem. Soc.* **2013**, *135*, 2291−2297.
(24) Lindahl, E.; Sansom, M. S. P. Membrane proteins: molecular dynamics simulations. *Curr. Opin. Struct. Biol.* **2008**, *18*, 425−431.
(25) Roux, B. Statistical mechanical equilibrium theory of selective ion channels. *Biophys. J.* **1999**, *77*, 139−153.
(26) Acevedo, O.; Jorgensen, W. L. Advances in quantum and molecular mechanical (QM/MM) simulations for organic and enzymatic reactions. *Acc. Chem. Res.* **2010**, *43*, 142−151.
(27) Hu, H.; Lu, Z.; Parks, J. M.; Burger, S. K.; Yang, W. Quantum mechanics/molecular mechanics minimum free-energy path for accurate reaction energetics in solution and enzymes: sequential sampling and optimization on the potential of mean force surface. *J. Chem. Phys.* **2008**, *128*, 034105.
(28) Li, W.; Rudack, T.; Gerwert, K.; Gräter, F.; Schlitter, J. Exploring the Multidimensional Free Energy Surface of Phosphoester Hydrolysis with Constrained QM/MM Dynamics. *J. Chem. Theory Comput.* **2012**, *8*, 3596−3604.
(29) Bentzien, J.; Muller, R. P.; Florián, J.; Warshel, A. Hybrid ab Initio Quantum Mechanics/Molecular Mechanics Calculations of Free Energy Surfaces for Enzymatic Reactions: The Nucleophilic Attack in Subtilisin. *J. Phys. Chem. B* **1998**, *102*, 2293−2301.
(30) Lennartz, C.; Schäfer, A.; Terstegen, F.; Thiel, W. Enzymatic reactions of triosephosphate isomerase: a theoretical calibration study. *J. Phys. Chem. B* **2002**, *106*, 1758−1767.
(31) Nam, K.; Prat-Resina, X.; Garcia-Viloca, M.; Devi-Kesavan, L. S.; Gao, J. Dynamics of an enzymatic substitution reaction in haloalkane dehylogenase. *J. Am. Chem. Soc.* **2004**, *126*, 1369−1376.
(32) Klähn, M.; Braun-Sand, S.; Rosta, E.; Warshel, A. On Possible Pitfalls in ab Initio Quantum Mechanics/Molecular Mechanics Minimization Approaches for Studies of Enzymatic Reactions. *J. Phys. Chem. B* **2005**, *109*, 15645−15650.
(33) Pettitt, B.; Karplus, M. Conformational Free Energy of Hydration for the Alanine Dipeptide: Thermodynamic Analysis. *J. Phys. Chem.* **1988**, *92*, 3994−3997.
(34) Roux, B. The calculation of the potential of mean force using computer simulations. *Comput. Phys. Commun.* **1995**, *91*, 275−282.
(35) Wereszczynski, J.; McCammon, J. A. Statistical mechanics and molecular dynamics in evaluating thermodynamic properties of biomolecular recognition. *Q. Rev. Biophys.* **2012**, *45*, 1−25.
(36) Torrie, G. M.; Valleau, J. P. Monte Carlo free energy estimates using non-Boltzmann sampling: Application to the sub-critical Lennard-Jones fluid. *Chem. Phys. Lett.* **1974**, *28*, 578−581.
(37) Torrie, G. M.; Valleau, J. P. Nonphysical sampling distributions in Monte Carlo free-energy estimation: Umbrella sampling. *J. Comput. Phys.* **1977**, *23*, 187−199.
(38) Hansen, H. S.; Hünenberger, P. H. Using the local elevation method to construct optimized umbrella sampling potentials: calculation of the relative free energies and interconversion barriers of glucopyranose ring conformers in water. *J. Comput. Chem.* **2010**, *31*, 1−23.
(39) Mezei, M. Adaptive umbrella sampling: Self-consistent determination of the non-Boltzmann bias. *J. Comput. Phys.* **1987**, *68*, 237−248.
(40) Bartels, C.; Karplus, M. Multidimensional adaptive umbrella sampling: applications to main chain and side chain peptide conformations. *J. Comput. Chem.* **1997**, *18*, 1450−1462.
(41) Bartels, C.; Karplus, M. Probability distributions for complex systems: adaptive umbrella sampling of the potential energy. *J. Phys. Chem. B* **1998**, *102*, 865−880.
(42) Yang, M.; MacKerell, A. D., Jr. Conformational sampling of oligosaccharides using Hamiltonian replica exchange with two-dimensional dihedral biasing potentials and the weighted histogram analysis method (WHAM). *J. Chem. Theory Comput.* **2015**, *11*, 788−799.
(43) Wojtas-Niziurski, W.; Meng, Y.; Roux, B.; Bernèche, S. Self-learning adaptive umbrella sampling method for the determination of

https://doi.org/10.1021/acs.jpca.1c00736
J. Phys. Chem. A 2021, 125, 4216−4232

free energy landscapes in multiple dimensions. *J. Chem. Theory Comput.* **2013**, *9*, 1885−1895.
(44) Kumar, S.; Bouzida, D.; Swendsen, R. H.; Kollman, P. A.; Rosenberg, J. M. The weighted histogram analysis method for free-energy calculations on biomolecules. I. The method. *J. Comput. Chem.* **1992**, *13*, 1011−1021.
(45) Boczko, E. M.; Brooks, C. L., III Constant-Temperature Free Energy Surfaces for Physical and Chemical Processes. *J. Phys. Chem.* **1993**, *97*, 4509−4513.
(46) Tan, Z.; Gallicchio, E.; Lapelosa, M.; Levy, R. M. Theory of binless multi-state free energy estimation with applications to protein-ligand binding. *J. Chem. Phys.* **2012**, *136*, 144102.
(47) Kästner, J.; Thiel, W. Bridging the gap between thermodynamic integration and umbrella sampling provides a novel analysis method: "Umbrella integration. *J. Chem. Phys.* **2005**, *123*, 144104.
(48) Kästner, J.; Thiel, W. Analysis of the statistical error in umbrella sampling simulations by umbrella integration. *J. Chem. Phys.* **2006**, *124*, 234106.
(49) Kästner, J. Umbrella integration in two or more reaction coordinates. *J. Chem. Phys.* **2009**, *131*, 034109.
(50) Shirts, M. R.; Chodera, J. D. Statistically optimal analysis of samples from multiple equilibrium states. *J. Chem. Phys.* **2008**, *129*, 124105.
(51) Li, P.; Jia, X.; Pan, X.; Shao, Y.; Mei, Y. Accelerated Computation of Free Energy Profile at ab Initio Quantum Mechanical/Molecular Mechanics Accuracy via a Semi-Empirical Reference Potential. I. Weighted Thermodynamics Perturbation. *J. Chem. Theory Comput.* **2018**, *14*, 5583−5596.
(52) Lee, T.-S.; Radak, B. K.; Pabis, A.; York, D. M. A new maximum likelihood approach for free energy profile construction from molecular simulations. *J. Chem. Theory Comput.* **2013**, *9*, 153−164.
(53) Lee, T.-S.; Radak, B. K.; Huang, M.; Wong, K.-Y.; York, D. M. Roadmaps through free energy landscapes calculated using the multidimensional vFEP approach. *J. Chem. Theory Comput.* **2014**, *10*, 24−34.
(54) Schofield, J. Optimization and Automation of the Construction of Smooth Free Energy Profiles. *J. Phys. Chem. B* **2017**, *121*, 6847−6859.
(55) Gaines, C. S.; Giese, T. J.; York, D. M. Cleaning Up Mechanistic Debris Generated by Twister Ribozymes Using Computational RNA Enzymology. *ACS Catal.* **2019**, *9*, 5803−5815.
(56) Ganguly, A.; Weissman, B. P.; Giese, T. J.; Li, N.-S.; Hoshika, S.; Rao, S.; Benner, S. A.; Piccirilli, J. A.; York, D. M. Confluence of theory and experiment reveals the catalytic mechanism of the Varkud satellite ribozyme. *Nat. Chem.* **2020**, *12*, 193−201.
(57) Gaines, C. S.; York, D. M. Model for the Functional Active State of the TS Ribozyme from Molecular Simulation. *Angew. Chem.* **2017**, *129*, 13577−13580.
(58) Ekesan, Ş.; York, D. M. Dynamical ensemble of the active state and transition state mimic for the RNA-cleaving 8−17 DNAzyme in solution. *Nucleic Acids Res.* **2019**, *47*, 10282−10295.
(59) Kostenbader, K.; York, D. M. Molecular simulations of the pistol ribozyme: unifying the interpretation of experimental data and establishing functional links with the hammerhead ribozyme. *RNA* **2019**, *25*, 1439−1456.
(60) Bevilacqua, P. C.; Harris, M. E.; Piccirilli, J. A.; Gaines, C.; Ganguly, A.; Kostenbader, K.; Ekesan, Ş.; York, D. M. An Ontology for Facilitating Discussion of Catalytic Strategies of RNA-Cleaving Enzymes. *ACS Chem. Biol.* **2019**, *14*, 1068−1076.
(61) Gaines, C. S.; Piccirilli, J. A.; York, D. M. The L-platform/L-scaffold framework: a blueprint for RNA-cleaving nucleic acid enzyme design. *RNA* **2020**, *26*, 111−125.
(62) Hub, J. S.; de Groot, B. L.; van der Spoel, D. g_wham − A Free Weighted Histogram Analysis Implementation Including Robust Error and Autocorrelation Estimates. *J. Chem. Theory Comput.* **2010**, *6*, 3713−3720.
(63) Huang, M.; Giese, T. J.; Lee, T.-S.; York, D. M. Improvement of DNA and RNA Sugar Pucker Profiles from Semiempirical Quantum Methods. *J. Chem. Theory Comput.* **2014**, *10*, 1538−1545.
(64) Huang, M.; Dissanayake, T.; Kuechler, E.; Radak, B. K.; Lee, T.-S.; Giese, T. J.; York, D. M. A Multidimensional B-Spline Correction for Accurate Modeling Sugar Puckering in QM/MM Simulations. *J. Chem. Theory Comput.* **2017**, *13*, 3975−3984.
(65) Huang, M.; Giese, T. J.; York, D. M. Nucleic acid reactivity: Challenges for next-generation semiempirical quantum models. *J. Comput. Chem.* **2015**, *36*, 1370−89.
(66) E, W.; Ren, W.; Vanden-Eijnden, E. Finite temperature string method for the study of rare events. *J. Phys. Chem. B* **2005**, *109*, 6688−6693.
(67) Mills, G.; Jónsson, H. Quantum and thermal effects in H_2 dissociative adsorption: Evaluation of free energy barriers in multidimensional quantum systems. *Phys. Rev. Lett.* **1994**, *72*, 1124−1127.
(68) Mills, G.; Jónsson, H.; Schenter, G. K. Reversible work transition state theory: application to dissociative adsorption of hydrogen. *Surf. Sci.* **1995**, *324*, 305−337.
(69) Giese, T. J.; York, D. M. *FE-ToolKit: The Free Energy Analysis Toolkit*. https://gitlab.com/RutgersLBSR/fe-toolkit.
(70) Milovanović, G. V.; Udovičić, Z. Calculation of coefficients of a cardinal B-spline. *Applied Mathematics Letters* **2010**, *23*, 1346−1350.
(71) Ding, X.; Vilseck, J. Z.; Brooks, C. L., III Fast Solver for Large Scale Multistate Bennett Acceptance Ratio Equations. *J. Chem. Theory Comput.* **2019**, *15*, 799−802.
(72) Press, W. H.; Teukolsky, S. A.; Vetterling, W. T.; Flannery, W. P. *Numerical Recipes in Fortran*, 2nd ed.; Cambridge University Press: Cambridge, 1992.
(73) Ding, X.; Vilseck, J. Z.; Hayes, R. L.; Brooks, C. L. Gibbs Sampler-Based λ-Dynamics and Rao-Blackwell Estimator for Alchemical Free Energy Calculation. *J. Chem. Theory Comput.* **2017**, *13*, 2501−2510.
(74) Zhang, B. W.; Xia, J.; Tan, Z.; Levy, R. M. A Stochastic Solution to the Unbinned WHAM Equations. *J. Phys. Chem. Lett.* **2015**, *6*, 3834−3840.
(75) Giese, T. J.; Panteva, M. T.; Chen, H.; York, D. M. Multipolar Ewald methods, 1: Theory, accuracy, and performance. *J. Chem. Theory Comput.* **2015**, *11*, 436−450.
(76) Hardy, R. L. Multiquadric equations of topography and other irregular surfaces. *J. Geophys. Res.* **1971**, *76*, 1905−1915.
(77) Fornberg, B.; Wright, G. Stable compution of multiquadric interpolants for all values of the shape parameter. *Comput. Math. with Appl.* **2004**, *48*, 853−867.
(78) Acar, E. Optimizing the shape parameters of radial basis functions: An application to automobile crashworthiness. *Proc. Inst. Mech. Eng., Part D* **2010**, *224*, 1541−1553.
(79) Fasshauer, G. E.; Zhang, J. G. On choosing "optimal" shape parameters for RBF approximation. *Numer. Algorithms* **2007**, *45*, 245−368.
(80) Perdew, J. P.; Ernzerhof, M.; Burke, K. Rationale for mixing exact exchange with density functional approximations. *J. Chem. Phys.* **1996**, *105*, 9982−9985.
(81) Adamo, C.; Scuseria, G. E.; Barone, V. Accurate excitation energies from time-dependent density functional theory: Assessing the PBE0 model. *J. Chem. Phys.* **1999**, *111*, 2889−2899.
(82) Horn, H. W.; Swope, W. C.; Pitera, J. W.; Madura, J. D.; Dick, T. J.; Hura, G. L.; Head-Gordon, T. Development of an improved four-site water model for biomolecular simulations: TIP4P-Ew. *J. Chem. Phys.* **2004**, *120*, 9665−9678.
(83) Giese, T. J.; York, D. M. Ambient-Potential Composite Ewald Method for ab Initio Quantum Mechanical/Molecular Mechanical Molecular Dynamics Simulation. *J. Chem. Theory Comput.* **2016**, *12*, 2611−2632.
(84) Maier, J. A.; Martinez, C.; Kasavajhala, K.; Wickstrom, L.; Hauser, K. E.; Simmerling, C. ff14SB: Improving the Accuracy of Protein Side Chain and Backbone Parameters from ff99SB. *J. Chem. Theory Comput.* **2015**, *11*, 3696−3713.
(85) Darden, T.; York, D.; Pedersen, L. Particle mesh Ewald: An N log(N) method for Ewald sums in large systems. *J. Chem. Phys.* **1993**, *98*, 10089−10092.

https://doi.org/10.1021/acs.jpca.1c00736
J. Phys. Chem. A 2021, 125, 4216−4232

(86) Essmann, U.; Perera, L.; Berkowitz, M. L.; Darden, T.; Lee, H.; Pedersen, L. G. A smooth particle mesh Ewald method. *J. Chem. Phys.* **1995**, *103*, 8577−8593.
(87) Martick, M.; Lee, T.-S.; York, D. M.; Scott, W. G. Solvent structure and hammerhead ribozyme catalysis. *Chem. Biol.* **2008**, *15*, 332−342.
(88) Chen, H.; Giese, T. J.; Golden, B. L.; York, D. M. Divalent Metal Ion Activation of a Guanine General Base in the Hammerhead Ribozyme: Insights from Molecular Simulations. *Biochemistry* **2017**, *56*, 2985−2994.
(89) Case, D. A.; Ben-Shalom, I. Y.; Brozell, S. R.; Cerutti, D. S.; Cheatham, T. E., III; Cruzeiro, V. W. D.; Darden, T. A.; Duke, R. E.; Ghoreishi, D.; Gilson, M. K. et al. *AMBER 18*. University of California: San Francisco, CA, 2018.
(90) Pérez, A.; Marchán, I.; Svozil, D.; Sponer, J.; Cheatham, T. E., III; Laughton, C. A.; Orozco, M. Refinement of the AMBER force field for nucleic acids: Improving the description of α/γ conformers. *Biophys. J.* **2007**, *92*, 3817−3829.
(91) Zgarbová, M.; Otyepka, M.; Šponer, J.; Mládek, A.; Banáš, P.; Cheatham, T. E., III; Jurečka, P. Refinement of the Cornell et al. nucleic acids force field based on reference quantum chemical calculations of glycosidic torsion profiles. *J. Chem. Theory Comput.* **2011**, *7*, 2886−2902.
(92) Joung, I. S.; Cheatham, T. E., III Determination of alkali and halide monovalent ion parameters for use in explicitly solvated biomolecular simulations. *J. Phys. Chem. B* **2008**, *112*, 9020−9041.
(93) Li, P.; Roberts, B. P.; Chakravorty, D. K.; Merz, K. M., Jr. Rational design of Particle Mesh Ewald compatible Lennard-Jones parameters for + 2 metal cations in explicit solvent. *J. Chem. Theory Comput.* **2013**, *9*, 2733−2748.
(94) Panteva, M. T.; Giambaşu, G. M.; York, D. M. Comparison of structural, thermodynamic, kinetic and mass transport properties of Mg^{2+} ion models commonly used in biomolecular simulations. *J. Comput. Chem.* **2015**, *36*, 970−982.
(95) Panteva, M. T.; Giambasu, G. M.; York, D. M. Force Field for Mg^{2+}, Mn^{2+}, Zn^{2+}, and Cd^{2+} Ions that have Balanced Interactions with Nucleic Acids. *J. Phys. Chem. B* **2015**, *119*, 15460−15470.
(96) Ryckaert, J. P.; Ciccotti, G.; Berendsen, H. J. C. Numerical Integration of the Cartesian Equations of Motion of a System with Constraints: Molecular Dynamics of n-Alkanes. *J. Comput. Phys.* **1977**, *23*, 327−341.
(97) Nam, K.; Cui, Q.; Gao, J.; York, D. M. Specific reaction parametrization of the AM1/d Hamiltonian for phosphoryl transfer reactions: H, O, and P atoms. *J. Chem. Theory Comput.* **2007**, *3*, 486−504.
(98) Rosta, E.; Nowotny, M.; Yang, W.; Hummer, G. Catalytic mechanism of RNA backbone cleavage by ribonuclease h from quantum mechanics/molecular mechanics simulations. *J. Am. Chem. Soc.* **2011**, *133*, 8934−8941.
(99) Ganguly, A.; Thaplyal, P.; Rosta, E.; Bevilacqua, P. C.; Hammes-Schiffer, S. Quantum Mechanical/Molecular Mechanical Free Energy Simulations of the Self-Cleavage Reaction in the Hepatitis Delta Virus Ribozyme. *J. Am. Chem. Soc.* **2014**, *136*, 1483−1496.
(100) Lee, T.-S.; López, C. S.; Giambaşu, G. M.; Martick, M.; Scott, W. G.; York, D. M. Role of Mg^{2+} in hammerhead ribozyme catalysis from molecular simulation. *J. Am. Chem. Soc.* **2008**, *130*, 3053−3064.
(101) Lee, T.-S.; Giambaşu, G. M.; Moser, A.; Nam, K.; Silva-Lopez, C.; Guerra, F.; Nieto-Faza, O.; Giese, T. J.; Gao, J.; York, D. M. Unraveling the Mechanisms of Ribozyme Catalysis with Multiscale Simulations. *Challenges Adv. Comput. Chem. Phys.* **2009**, *7*, 377−408.
(102) Lee, T.-S.; York, D. M. Computational mutagenesis studies of hammerhead ribozyme catalysis. *J. Am. Chem. Soc.* **2010**, *132*, 13505−13518.
(103) Wong, K.-Y.; Lee, T.-S.; York, D. M. Active participation of the Mg^{2+} ion in the reaction coordinate of RNA self-cleavage catalyzed by the hammerhead ribozyme. *J. Chem. Theory Comput.* **2011**, *7*, 1−3.
(104) Ganguly, A.; Weissman, B. P.; Piccirilli, J. A.; York, D. M. Evidence for a Catalytic Strategy to Promote Nucleophile Activation in Metal-Dependent RNA-Cleaving Ribozymes and 8−17 DNAzyme. *ACS Catal.* **2019**, *9*, 10612−10617.
(105) Huang, M.; York, D. M. Linear free energy relationships in RNA transesterification: theoretical models to aid experimental interpretations. *Phys. Chem. Chem. Phys.* **2014**, *16*, 15846−15855.
(106) Chen, H.; Giese, T. J.; Huang, M.; Wong, K.-Y.; Harris, M. E.; York, D. M. Mechanistic Insights into RNA Transphosphorylation from Kinetic Isotope Effects and Linear Free Energy Relationships of Model Reactions. *Chem. - Eur. J.* **2014**, *20*, 14336−14343.
(107) Hengge, A. C. Isotope effects in the study of phosphoryl and sulfuryl transfer reactions. *Acc. Chem. Res.* **2002**, *35*, 105−112.
(108) Weissman, B. P.; Li, N.-S.; York, D. M.; Harris, M.; Piccirilli, J. A. Heavy atom labeled nucleotides for measurement of kinetic isotope effects. *Biochim. Biophys. Acta, Proteins Proteomics* **2015**, *1854*, 1737−1745.
(109) Kellerman, D. L.; York, D. M.; Piccirilli, J. A.; Harris, M. E. Altered (transition) states: mechanisms of solution and enzyme catalyzed RNA 2′-O-transphosphorylation. *Curr. Opin. Chem. Biol.* **2014**, *21*, 96−102.
(110) Harris, M. E.; Piccirilli, J. A.; York, D. M. Integration of kinetic isotope effect analyses to elucidate ribonuclease mechanism. *Biochim. Biophys. Acta, Proteins Proteomics* **2015**, *1854*, 1801−1808.
(111) Towns, J.; Cockerill, T.; Dahan, M.; Foster, I.; Gaither, K.; Grimshaw, A.; Hazlewood, V.; Lathrop, S.; Lifka, D.; Peterson, G. D.; et al. XSEDE: Accelerating Scientific Discovery. *Comput. Sci. Eng.* **2014**, *16*, 62−74.

https://doi.org/10.1021/acs.jpca.1c00736
J. Phys. Chem. A 2021, 125, 4216−4232